PERFORMANCE OPTIMIZATION OF SWITCHED RELUCTANCE MOTOR DRIVE USING META-HEURISTIC TECHNIQUE

MAJOR PROJECT II

REPORT

SUBMITTED IN PARTIAL FULFILLMENT OF THE

REQUIREMENTS FOR THE AWARD OF THE DEGREE

OF

MASTER OF TECHNOLOGY

IN

ELECTRICAL ENGINEERING

Submitted By:

MOHD FARHANUDDIN

2K20/PSY/13

Under the Supervision of

Dr. Suman Bhowmick **Mr. Sikandar Ali Khan**

DEPARTMENT OF ELECTRICAL ENGINEERING

DELHI TECHNOLOGICAL UNIVERSITY

(Formerly Delhi College of Engineering)

Bawana Road, Delhi - 110042

JUNE 2022

CANDIDATE'S DECLARATION

I, MOHD FARHANUDDIN, Roll No. 2K20/PSY/11, a student of M. Tech (Electrical Engineering), hereby declare that the report titled "Performance Optimization of Switched Reluctance Motor Drive using Meta-Heuristic Technique " which is submitted by me to the Department of Electrical Engineering, Delhi Technological University, Delhi, in partial fulfillment of the requirement for the award of the degree of Master of Technology, is original and not copied from any source without proper citation. This work has not previously formed the basis for the award of any Degree, Diploma, Associateship, Fellowship or another similar title of recognition.

Place: New Delhi

Date: 30th May 2022

CERTIFICATE

I hereby certify that the report titled "Performance Optimization of Switched Reluctance Motor Drive using Meta-Heuristic Technique" which is submitted by MOHD FARHANUDDIN, 2K20/PSY/13, Department of Electrical Engineering, Delhi Technological University, Delhi inpartial fulfillment of the requirement for the award of the degree of Master ofTechnology, is a record of the project work carried out by the student under my supervision. To the best of my knowledge this work has not been submitted in part or full for any Degree or Diploma to this University or elsewhere.

Place: New Delhi

Date: 30th May 2022

Dr. Suman Bhowmick
(Supervisor)

Mr. Sikandar Ali Khan
(Co- supervisor)

ACKNOWLEDGMENT

I wish to express my profound gratitude and indebtedness to **Dr. Suman Bhowmick**, Professor, Department of Electrical Engineering, Delhi Technological University, New Delhi, and **Mr. Sikandar Ali Khan** Assistant Professor, Department of Electrical Engineering, Delhi Technological University, New Delhi for introducing the present topic and for their inspiring guidance, constructive criticism, and valuable suggestions throughout this project work.

I would also express my gratitude to all the professors of the Department of Electrical Engineering, Delhi Technological University, New Delhi, for their guidance and the support they have provided to me.

Lastly, my sincere thanks to all of my friends, parents who have patiently extended all sorts of help for accomplishing this undertaking.

MOHD FARHANUDDIN

2k20 / PSY / 13

Department of Electrical Engineering
Delhi Technological University, New Delhi

ABSTRACT

This thesis presents a population centric teaching-learning based optimisation (TLBO) technique for optimizing the performance of switched reluctance motor (SRM) drives. SRMs have proven to be a good substitute of Permanent Magnet (PM) motors despite minor disadvantages like noise, vibration, and torque ripple. In this work, TLBO is used to compute the turn-on and turn-off angles of the stator phase windings to optimise a multi-objective function comprising the SRM drive performance indices like average torque, torque per unit copper loss and softness factor (inverse of the torque ripple factor) while subjecting the drive to the Indian Drive Cycle (IDC). Two real time controllers have been used to tune the turn-on and turn-off angles of the stator phase windings. The optimal turn-on and turn-off angles are used to generate the gate pulses for the converter switches. A hysteresis controller is incorporated to regulate the stator current between prescribed limits. The entire model was developed in SIMULINK. The improved SRM performance indices show the effectiveness of the proposed controller.

TABLE OF CONTENTS

CHAPTER 3 : CONTROL OF SRM

CHAPTER 4 : COMPOSITE SYSTEM MODELLING

CHAPTER 5 : CASE STUDY AND RESULTS

LIST OF FIGURES

CHAPTER 1: INTRODUCTION AND LITERATURE REVIEW

1.1 Introduction:

When compared to Permanent Magnet Synchronous Motors (PMSM) and Induction motors, SRM is proven to be a tough contender in the era of motor drive technology due to its basic and sturdy architecture. SRM is a machine that has saliency on both the rotor and the stator. As shown in Figure 1.1, the stator has a laminated core with concentrated windings, whereas the rotor has no windings or Permanent Magnet. Because there is no rotor winding, the motor may run at extremely high speeds. At high speeds, rotor displacement and rotational stresses can severely limit PMSM motor dynamics. The radial force created as the rotor rotates at high speeds creates significant stresses on the magnet slots and bridges. Bridges are the areas of the rotor center between the magnet opening and the air gap. They must be constructed with great care to withstand radial forces. Strong rotor cores with no slots or bridges are used in SRMs. Despite some drawbacks such as noise, vibration, and torque ripples, this makes SRMs great candidates for high-speed applications. Currently, in light of increasing pollution and depleting fossil-fuel reserves, the automobile industry is slowly but surely inching towards renewable energy-based vehicles from conventional ones. As a result, electric vehicles (EVs) are increasingly being used, being a non-polluting and cost-effective solution.

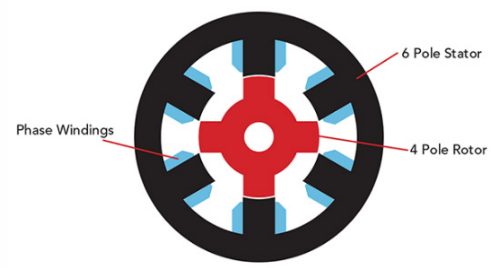

Figure 1.1 6/4 SRM

In Indian roads, the vehicle type is heterogeneous, including cyclists, mopeds, two and three wheelers, commercial transport, and buses etc. The Indian Drive Cycle (IDC) was developed by the scientists at the Automotive Research Association of India, Pune in 1985 after collecting real world data from major cities representing actual driving pattern. For the past few years, numerous research is being carried out to make EVs better than conventional IC engine-based vehicles in terms of acceleration and maneuverability. Major challenges exist in the use of rare earth metals in EV motor for satisfactory operation. In this respect, SRMs offer a simple and rugged design and do not contain any rare earth metals.

1.2 Literature Review:

[1]-[14] offer a number of comprehensive research studies on SRMs. [1]-[2] demonstrate the competitiveness of SRMs versus PM motors. [3]-[6] deal with the modelling, design, and analysis of SRMs. Moreover, various studies have sought to maximize SRM performance for motoring applications. However, the majority of these studies [6]-[10] concentrated on single-objective optimization and ignored aspects such as average torque maximization and loss minimization. The torque profile was improved using the Genetic Algorithm (GA) in [10]. To eliminate ripples in the torque profile, [11] adopted a new converter topology called the modular multilevel converter (MMC). To increase the overall performance of SRMs, multi-objective optimization is required. Particle Swarm Optimization (PSO) is used in [12] to maximize torque per active mass, efficiency, and torque ripple. [13] presented a more advanced optimization technique called TLBO. It is parameter-agnostic, needs less computational effort, and has a high level of consistency. This study presents a TLBO-based method for computing the stator phase windings' turn-on and turn-off angles in order to maximize a multi-objective function that includes average torque, torque per unit copper loss, and softness factor. The stator phase windings' turn-on and turn-off angles were tuned using two real-time controllers. The gate pulses for the converter switches are generated using the optimal turn on and turn off angles.

Also, this thesis shows how the Indian Drive Cycle (IDC) can be used in an SRM drive. Similarly, the best turn-on and turn-off angles of the stator phase windings are computed and gate pulses for the converter switches are generated using the same metaheuristic technique. This is done to optimize a multi-objective function that includes SRM drive performance indices such average torque, stator copper losses, and the motor and reference speeds' integral squared error. The stator current is regulated between set limits by a hysteresis controller. The motor is observed to track the drive cycle speed satisfactorily while optimizing the drive performance indices. The proposed technique's efficiency is confirmed by simulation results.

CHAPTER 2: DESIGN OF SRMs

2.1 Introduction:

Performance analysis of the SRM requires the dimensions for stator and rotor laminations, winding details, pole numbers, and pole arcs. An approximate sizing of the SRM is obtainable using a power output equation familiar to machine designers. The resulting machine dimensions form the starting point in design evaluation, and final design is achieved through an iterative process of steady-state performance calculations described in this chapter. This chapter contains the derivation of the output equation and selection of various machine variables such as number of poles, rotor and stator pole arcs, core length, bore diameter, back iron thickness, number of turns in each phase, and air gap for rotary switched reluctance machines. The design trade-offs emerging from conflicting requirements are discussed in detail.

A procedure to calculate resistive and core losses is presented. Flux densities at various parts of the machine are derived from first principles. Measurement of winding inductance is crucial to the validation of machine design and is briefly described here. The computation of torque for ideal and practical currents is developed, and the procedure is equally applicable to both steady-state and dynamic processes.

A step-by-step design of linear motion SRMs is considered in detail. To utilize the knowledge base of the rotary SRM, the linear machine design is achieved using the rotary SRM design process developed in this chapter. To accomplish it, the design specifications of the linear machine are converted to rotary machine design specifications. Then, an equivalent rotary SRM is designed, and the design outcomes are translated into linear machine dimensions and variables by simple algebraic relationships. The design verification with analysis using magnetic equivalent circuits, finite element method, and experimental measurements is developed in detail. The procedure for inductance and force measurements is also described in this chapter for the linear SRM.

2.2 Mathematical Analysis:

The output equation connects a machine's output to its bore diameter, length, speed, and magnetic and electric loadings. In general, traditional machines are built with the output equation in mind. SRM's design will be more systematic if the output equation is developed similarly. Furthermore, the machine designers' experience can be efficiently employed in the design of these new machines since they can start with the similarities between these and traditional machines.

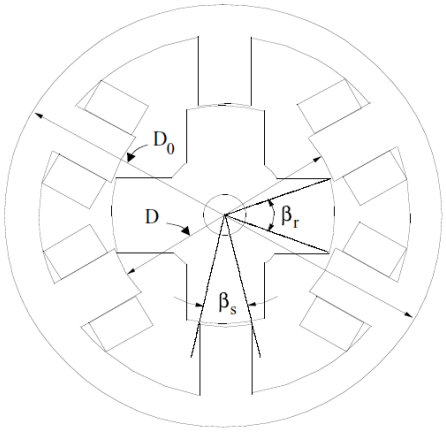

Figure 2.1: A 6/4 SRM with Mathematical Parameter.

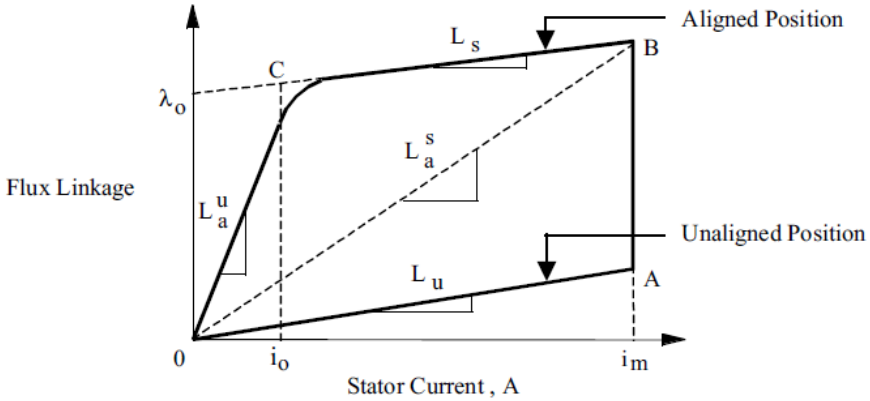

Figure 2.2: Flux linkage vs. Stator Current for SRM.

Figure 2.1 depicts an SRM with six stator poles and four rotor poles. Figure 2.2 depicts the flux linkages vs. current characteristics for the stator and rotor poles in their unaligned and properly aligned positions. Because the stator and rotor poles are misaligned, the stator pole's centre is sandwiched between the two rotor poles. The area surrounded by OABCO represents the motor's output mechanical energy for a single stroke. The applied voltage equals the rate of change of flux linkages when the resistive voltage drop in the machine winding is ignored. Then, by ignoring resistive voltage drop, the flux linkage–voltage relationship for a flat-topped phase current I is found as:

$$V \cong \frac{d\lambda}{dt} = \frac{\lambda_a - \lambda_u}{\lambda_u} = \frac{(L_a^S - L_u)\, i}{t} \qquad (2.1)$$

where L_a^S as is the aligned saturated inductance per phase, $L_u$is the unaligned saturated inductance per phase, V is the applied voltage, and t is the time it takes the rotor to change from unaligned to aligned. In terms of stator pole arc and rotor speed, that time may be expressed as:

$$t = \frac{\beta_s}{\omega_m} \tag{2.2}$$

where β_s is the stator pole arc in rad, and ω_m is the rotor speed in rad/s

We define:

$$\sigma_s = \frac{L_a^s}{L_a^u} \tag{2.3}$$

and

$$\sigma_u = \frac{L_a^u}{L_u} \tag{2.4}$$

where L_a^s is the aligned but unsaturated inductance. Substituting Eqs. (2.3) and (2.4) in Eq. (2.1), the applied voltage becomes:

$$V = \frac{\omega_m}{\beta_s} L_a^s i \left(1 - \frac{1}{\sigma_s \sigma_u}\right) \tag{2.5}$$

We write the flux linkages in the aligned position in terms of flux and number of turns and then in terms of flux density and machine dimensions as:

$$L_a^s i = \phi T_{ph} = B \times A_{sp} \times T_{ph} = B \times D \times L \times \beta_s \times T_{ph}/2 \tag{2.6}$$

where ϕ is the aligned flux, *Asp* is the area of the stator pole, *D* is the bore diameter, *L* is the axial length of the stator pole, *B* is the stator pole flux density at the aligned position, and T_{ph} is the number of turns per phase. The stator current may be obtained from the specific electric loading As, which is defined as:

$$A_s = \frac{2 T_{ph} i m}{\pi D} \tag{2.7}$$

where *m* is the number of phases conducting simultaneously. In the case of a 6/4 motor, such as the example being considered, only one phase conducts at a time.

The power developed then is,

$$P_d = k_e * k_d (V)(i)(m) \tag{2.8}$$

where V and i are peak phase values, k_d is the duty cycle defined in Eq. (2.9), and k_e is the efficiency. The duty cycle can be expressed as:

$$k_d = \frac{\theta_i \cdot qP_r}{360} \tag{2.9}$$

where θ_i is the current conduction angle for each rising inductance profile, q is the number of stator phases given by P_s /2, P_s is the number of stator poles, and P_r is the number of rotor poles.

Combining Eqs. (2.5) and (2.6), the power developed is given by:

$$P_d = k_e \cdot k_d \left(\frac{\pi^2}{120}\right)\left(1 - \frac{1}{\sigma_s \sigma_u}\right) BA_s D^2 L N_r \tag{2.10}$$

where N_r is the rotor speed in revolutions per minute (rpm). Equation (2.10) can be rearranged to resemble that of the conventional output equation of ac machines and is given by:

$$P_d = k_c k_d k_1 k_2 BA_s D^2 L N_r \tag{2.11}$$

where

$$k_1 = \frac{\pi^2}{120} \tag{2.12}$$

$$k_2 = 1 - \frac{1}{\sigma_s \sigma_u} \tag{2.13}$$

The torque can be obtained from Eq. (2.10) and expressed as:

$$T = k_d k_e k_3 k_2 \cdot (BA_s) D^2 L \tag{2.14}$$

where

$$k_3 = \frac{\pi}{4} \tag{2.15}$$

It's worth noting that the torque and power output are proportional to the product of specific electric and magnetic loadings, as well as bore volume $(\pi D^2 L)/4$. The sole variable that is reliant on the motor's operating point is k_2, which is dictated by the stator phase current, magnetic properties of the core materials, and the motor's size. k_2 is a constant at any operating point. As a result, k_2 must be computed at the maximum stator current in order to obtain the maximum output power from the SRM. In fact, for varied amounts of stator currents, the flux linkages vs. current for aligned and unaligned positions must be computed. For a given stator current, the power generated is highest when k_d =1.

The highest achievable duty cycle is almost always less than one. In addition, like a chopper-controlled dc motor, the duty cycle controls torque and output. The frequency of phase switching, similar to that of a synchronous motor, controls the speed.

2.3 Motor Sizing:

2.3.1 Diameter and Length:

Because the SRM is typically employed as a variable-speed device, a base speed specification is necessary. The motor is anticipated to deliver the rated torque and thus the rated output power at the base speed. The following is obtained using Eq. (2.11) to correlate to the rated power output and retaining the stack length as a multiple or submultiple of the rotor bore diameter:

$$L = k.D \tag{2.16}$$

which on substitution in the output power equation results in:

$$P_d \propto k_d \,.D^3 \tag{2.17}$$

From Eq. (3.17), D is evaluated if the rated speed B, A_{sp} ,k_2 , k_d, and k are known. It is possible to start the iterative process of design with reasonable values. In general, at the rated operating point, the range of $k2$ is given by:

$$0.65 < k_2 < 0.75 \tag{2.18}$$

The values of B for the aligned position can be taken as the allowable maximum for the core material. The specific electric loading in amp-conductors per meter is usually in the range of:

$$25000 < As < 90000 \tag{2.19}$$

To begin with, the duty cycle k_d might be considered to be one. Bore diameter D is calculated using the above beginning values. The air gap is dictated by the manufacturing techniques used and the limits they impose. Air gaps in small machinery range from 0.18 to 0.25 mm. Air gaps in integral horsepower machines can range from 0.3 to 0.5 mm. The lengths to bore k ratio does not have to be random; it is determined by the type of the application and space restrictions. The range of k can be extended for non-servo applications.

$$0.25 < k < 0.70 \tag{2.20}$$

and for servo applications it is usually in the range given by:

$$1 < k < 3 \tag{2.21}$$

2.3.2 Number of Turns:

For a given current, Eq. (2.7) is used to compute the number of turns per phase, T_{ph}. The conductor size is designed to fill all of the available winding space. The resulting current density is calculated and compared to the maximum permitted value, which is determined by the motor's cooling measures. If the outer diameter is unrestricted, the winding space can be determined using the number of turns, the conductor's area of cross-section, and the insulation thickness. The winding space is then used to calculate the stator pole's height. It can be seen from Eq. (2.7) that the product of T_{ph} and I is a constant for a given particular electric loading and bore diameter. The best values are those that satisfy the following set of mutually exclusive requirements:

1. A smaller current indicates a greater number of spins.
2. The winding's resistance and inductance are low, implying a low number of turns.

Thermal concerns must be considered when making an engineering trade-off. The choice of I and Tph is also reliant on the ac supply available for rectification and subsequent input to the converter to operate the SRM, as previously stated.

1.3.3 Thermal Analysis:

One of the most significant qualities is the motor's thermal capability. The thermal capability of a machine is defined by the machine's losses, the available cooling surface area, and any additional cooling arrangements such as a fan, a blower, or water- or liquid-circulated cooling. The next sections evaluate copper and core losses in order to calculate the machine's thermal rating.

1.3.3.1 Stator Copper Loss:

If *Rs* is the per-phase resistance of the stator winding, the total copper losses for non-overlapping currents in the stator is given by:

$$P_{cu} = q.\ I_2.\ R_s \tag{2.22}$$

where q is the number of stator phases, and I is the rms value of the current given by:

$$I = \frac{I_p}{\sqrt{q}} \tag{2.23}$$

where I_p is the peak value of phase current. Hence, the copper losses are

$$P_{cu} = I_p^2\ .\ R_s \tag{2.24}$$

We can write the resistance in terms of the number of turns and area of cross section of the conductor as:

$$R_s = \rho \cdot \frac{\ell}{a_c} = K_r \cdot \frac{T_{ph}}{a_c} \tag{2.25}$$

where a_c is the area of cross section of the conductor, ρ is the specific resistivity, l is the total length of the winding, K_r is the product of the resistivity, and the mean length of turn given by l_m.

Substituting Eq. (2.25) in (2.24),

$$P_{cu} = K_r\left(\frac{I_p}{a_c}\right)(T_{ph}i) \tag{2.26}$$

In terms of the current density given by

$$J_c = \frac{I_p}{a_c} \tag{2.27}$$

the copper losses are derived as:

$$P_{cu} \infty (J_c)(T_{ph} I_p) \tag{2.28}$$

Copper losses are proportional to current density since the maximum (T_{ph}. I_p) is a constant for a design. It should be noted that in order to reduce copper losses, the current density must be reduced. Consider the situation where phase currents overlap with both previous and subsequent phases. In an SRM drive, this is the most realistic scenario. Figure 2.3 shows the phase currents for a three-machine system with no switching transients and a linear rise and fall. It's worth noting that the copper losses in the stator at any one time are the sum of the copper losses caused by the instantaneous phase currents.

When the phase inductance varies and just a constant current is sought for the period T_{pc}, this equates to building the equivalent rms current in a phase for the time duration T_{pc}, as provided by:

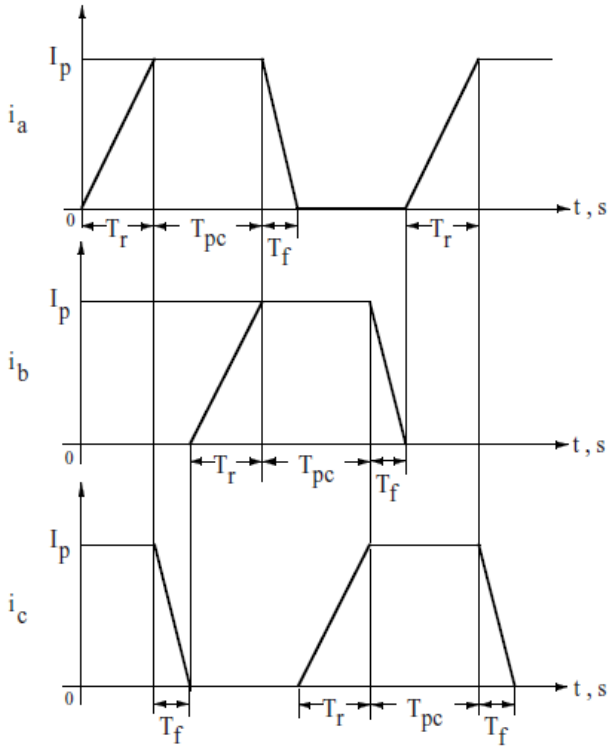

FIGURE 2.3 Typical but simplified stator currents with an overlap in a 6/4 SRM.

$$T_{pc} = \frac{\theta_{pc}}{\omega_m} = \frac{2\pi}{\left(\frac{P_s P_r}{2}\right)\omega_m} = \frac{4\pi}{\omega_m P_s P_r}, s \tag{2.29}$$

During this time interval, one phase's maximum current is believed to remain constant, the current in the preceding phase is declining, and the current in the following phase is rising. The combined effect of all three currents results in resistive losses, which are calculated as follows:

$$P_{cu} = I^2 \cdot R_s = \frac{R_s}{T_{pc}}\left[I_p^2 T_{pc} + \frac{1}{3}I_p^2 T_r + \frac{1}{3}I_p^2 T_f\right] = I_p^2 R_s\left[1 + \frac{(T_r + T_f)}{3T_{pc}}\right], W \quad (2.30)$$

The current rising and fall times are T_r and T_f, respectively. The equivalent circuit of the SRM can be used to approximate the values of T_r and T_f, The copper losses are dependent on speed when T_{pc} is substituted for in terms of speed and stator and rotor poles from Eq. (2.29) into Eq. (2.30). As a result, only the copper loss at the highest machine speed must be considered. This is critical for the machine's thermal design.

1.3.3.2 Calculation Of Core Losses:

The prediction of core loss is critical in the design of the machine and the assessment of its thermal rating. The sources of machine losses, as well as the correlations between lamination material qualities, machine dimensions, excitation conditions, and losses, are required for machine efficiency optimization. The evaluation of stator resistive losses in an SRM is reasonably straightforward, as previously stated, but core losses in the SRM are difficult to anticipate due to the occurrence of flux densities with varying frequencies in stator segments. Furthermore, neither the flux densities nor the sinusoids are pure sinusoids or constants.

Hysteresis and eddy current losses are the core losses of an SRM. The stator and rotor cores are laminated to prevent eddy current losses. The extent of hysteresis losses is determined by the frequency of flux reversal and its path. The flux densities in various channels of the machine are the first step in calculating machine core losses. Ps segments in the back iron and Ps in the poles make up the flux route segments in the stator. Poles and back iron make up the segments of the rotor laminations. Only two stator poles and two rotor poles carry the flux in one-phase excitation, with the entire stator back iron and the back iron of the non-flux-carrying poles in the rotor contributing to the flux path.

For a q-phase SRM, the number of unique iron segments is calculated as follows:

$$J = q + 2 \quad (2.31)$$

For non-overlapping stator currents, the total number of iron segments in use at any given time is:

$$k = 2q + 6 = 2\,(j+1) \quad (2.32)$$

If B_j is the flux density in the iron's j segment, then B_k can be used to calculate the flux density in the k portion. As a result of this process, flux density waveforms for various segments of the SRM can be derived graphically. For a three-phase SRM with six stator and four rotor poles, several

segments of the machine are depicted in Figure 2.4.

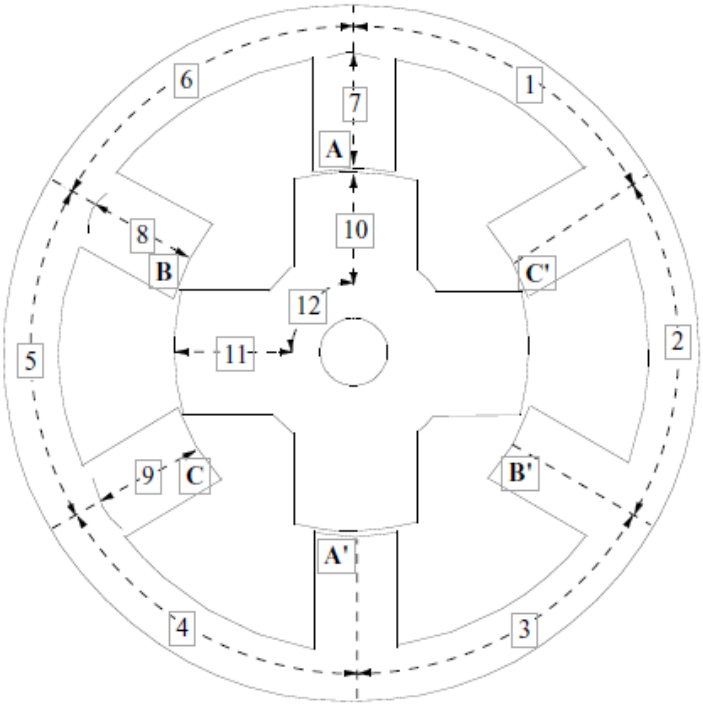

FIGURE 2.4 Iron segments in a 6/4 SRM.

1.3.4 Waveforms of Flux Density:

2.3.4.1 Stator:

Starting with the stator poles, the flux densities in various iron segments are calculated. Figure 2.5 shows the flux density of stator poles A and B_7 vs. rotor position. Other poles' flux densities are same, but phase shifted by θ_s. (i.e., the delay angle between phases when energizing the corresponding phase windings). Each phase current conducts for θ_c (conduction angle) seconds before falling to zero for θ (fall angle) duration. T Although the conduction and fall angles are not always identical, they are assumed to be equal in the following discussion for the sake of demonstration. The stator back iron segment flux density, B1, is proportional to the total of the stator pole flux densities (i.e., $B_7 + B_8 + B_9$). The rotor pole pitch θ_{rp} is calculated as follows:

$$\theta_{rp} = \frac{2\pi}{P_r} \tag{2.33}$$

Phase current displacement angle θ_s in terms of θ_{rp} is

$$\theta_s = \frac{\theta_{rp}}{(P_s/2)} = \frac{\theta_{rp}}{q} \tag{2.34}$$

The flux density in stator pole segment B_7 is

$$B_7 = \begin{cases} B_m \dfrac{\theta}{\theta_c}, & 0 \le \theta \le \theta_c \\ B_m \left[1 - \dfrac{(\theta - \theta_c)}{\theta_f}\right], & \theta_c \le \theta \le (\theta_c + \theta_f) \end{cases} \tag{2.35}$$

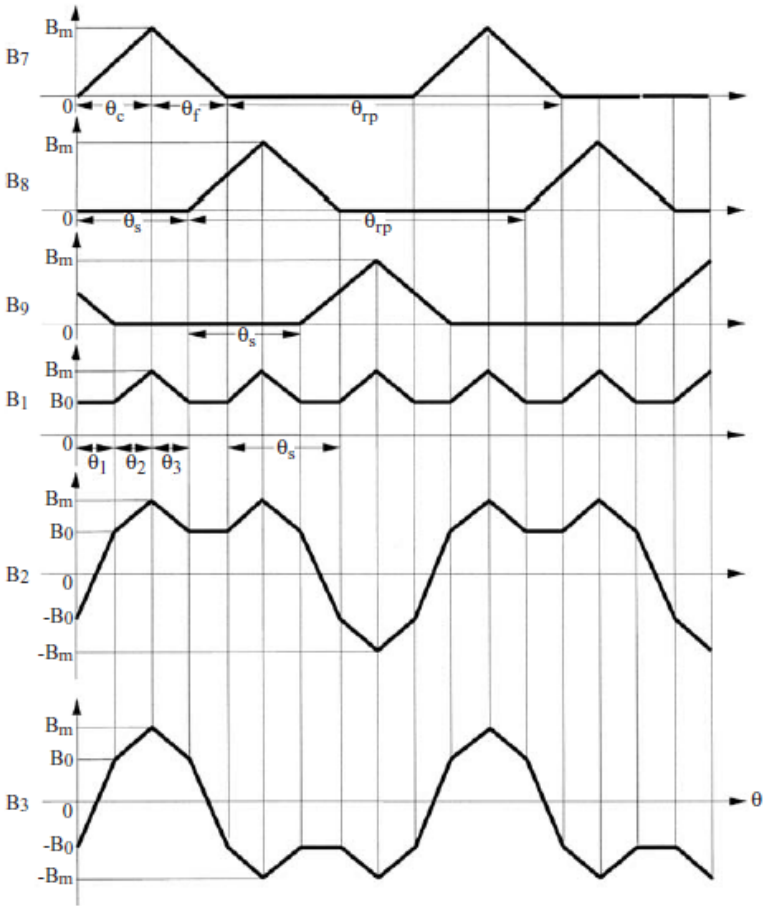

Figure 2.5 Stator flux density for 6/4 SRM shown in Figure 2.4.

For each θ_s radians, the flux density in the back iron section close to the stator pole, B_1, is repetitive and can be compactly represented as:

$$B_1 = \begin{cases} aB_m\left[\dfrac{\theta}{\theta_c} + \dfrac{\theta_f - (\theta + \theta_s - \theta_c)}{\theta_f}\right], & 0 \le \theta \le \theta_1 \\ aB_m\dfrac{\theta}{\theta_c}, & \theta_1 \le \theta \le \theta_c \\ aB_m\left[\dfrac{\theta_f - (\theta - \theta_c)}{\theta_f}\right], & \theta_c \le \theta \le \theta_s \end{cases} \tag{2.36}$$

where a is a constant that accounts for the area of cross-section differential in order to give a lower flux density in the stator core than in the stator poles to reduce acoustic noise in the SRM.

It's worth noting that:

$$\theta_1 = \theta_c + \theta_f - \theta_s \tag{2.37}$$

$$\theta_2 = \theta_c - \theta_1 \tag{2.38}$$

$$\theta_3 = \theta_s - \theta_c \tag{2.39}$$

$$\theta_s = \theta_1 + \theta_2 + \theta_3 \tag{2.40}$$

$$B_0 = aB_m\left[\frac{\theta_c + \theta_f - \theta_s}{\theta_c}\right] \tag{2.41}$$

The flux density in stator back iron segments 2 and 3 are derived as:

$$B_2 = a(B_7 + B_8 - B_9) \tag{2.42}$$

$$B_3 = a(B_7 - B_8 - B_9) \tag{2.43}$$

Note that from symmetry it can be shown that:

$$B_4 = B_1 \tag{2.42}$$

$$B_5 = B_2 \tag{2.43}$$

$$B_6 = B_3 \tag{2.44}$$

Even though B_2 and B_3 are similar, they are not identical. They have the same frequency, as given by:

$$f_2 = f_3 = \frac{\omega_m}{\theta_{rp}} = \frac{2\pi n_r}{(2\pi/P_r)} = n_r P_r \tag{2.45}$$

where n_r is the rotor speed in revolutions per second. The frequency of B_1 is

$$f_1 = \frac{\omega_m}{\theta_s} = \frac{2\pi n_r}{2\pi/(qP_r)} = qP_r n_r = qf_2 \tag{2.46}$$

The frequency of the stator pole flux density is given by:

$$f_7 = \frac{\omega_m}{\theta_{rp}} = n_r P_r = f_2 \tag{2.47}$$

There are m different flux intensities in the stator, including its poles and back iron segments, for a machine with phases larger than or equal to 3. While B_1, B_7, B_8, and B_9 have unidirectional flux densities, they also feature ripples, which cause core losses to increase. Both B_2 and B_3 are bidirectional, resulting in substantially higher core losses.

2.3.4.2 Rotor:

For an q-phase SRM with Pr rotor poles, each pair of rotor poles aligns with a pair of stator poles at a periodic interval given by:

$$\theta_{r1} = \frac{(q-1)}{q} \cdot \theta_{sp} = (q-1)\theta_s \tag{2.48}$$

where θ_{sp} is the stator pole pitch given as:

$$\theta_{sp} = \frac{2\pi}{P_s} = \frac{\theta_s \cdot P_r}{2} \tag{2.49}$$

The rotor pole flux reverses every half a revolution of the rotor. Over a complete revolution, the rotor pole flux density waveform shown as B_{10} in Figure 2.6 is a bipolar envelope with a frequency:

$$f_{10} = \frac{\omega_r}{2\pi} = n_r \tag{2.50}$$

But it has a carrier (ripple) content whose frequency is given by:

$$f_{10r} = 2qn_r = n_r . P_s \tag{2.51}$$

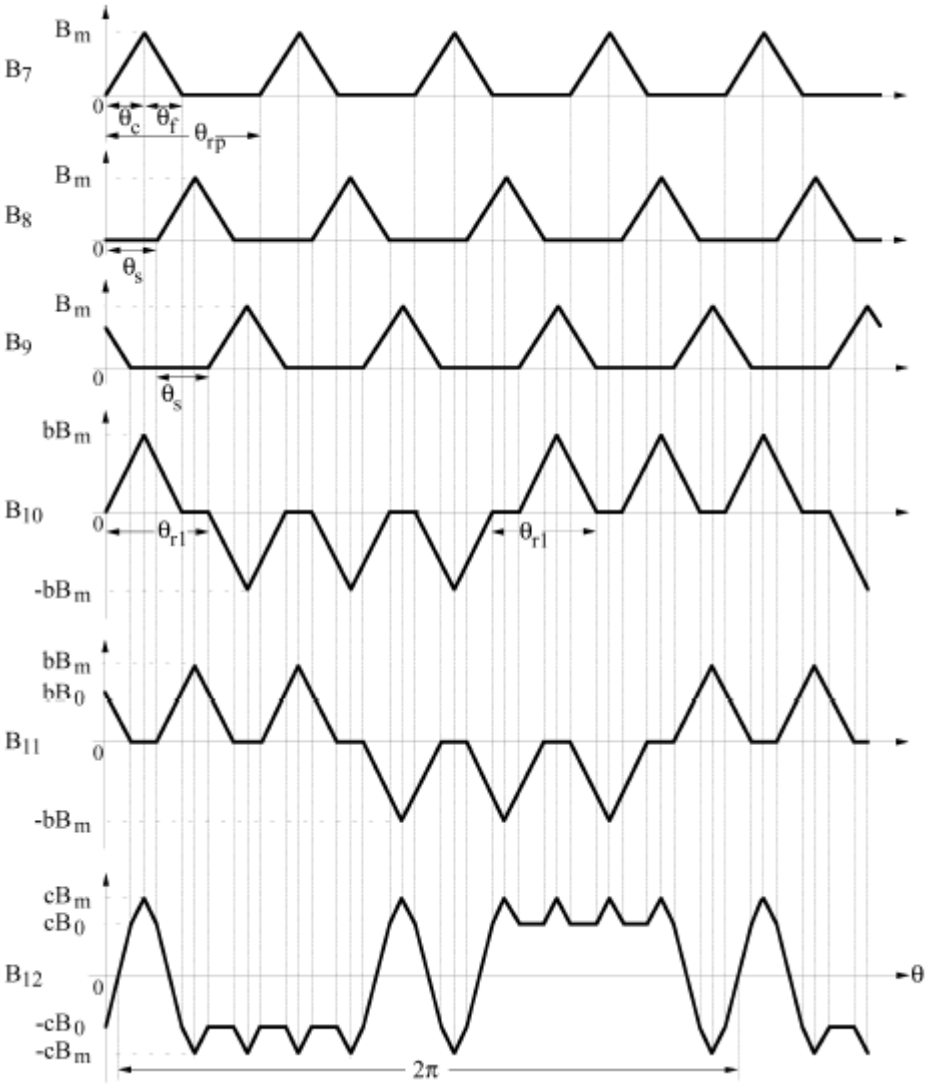

Figure 2.6 Rotor flux density waveforms of the 6/4 SRM.

To account for the difference in stator and rotor pole cross-sectional area, the rotor pole flux density peak is bB_m. For the rotor pole core portion, a factor θc has also been introduced.

2.3.4.5 Core Losses:

A method based on Steinmetz's equations for eddy current losses and Preisach's model for hysteresis losses is a viable approach that uses a physical understanding of associating machine characteristics and variables analytically to the losses. A simplified approach for calculating core losses is described below for the sake of simplicity. It should be noted that it can be used for a rough estimate but not for situations that demand precision in forecasting efficiency or thermal rise. Then it's time to use finite element analysis (FEA).

CHAPTER 3: CONTROL OF SRM

3.1 Introduction:

While SRMs and other electric machines have many similarities, the principles that govern their control set them apart from other machine topologies. The unique geometry and torque generating mechanism of SRMs sets them apart from typical machine topologies, which makes modelling the motor difficult. The machine's doubly salient form causes substantial changes in the air gap, resulting in a non-linear machine flux linkage as a function of rotor position. SRMs also work in a magnetically saturated environment. Modelling and controlling the machine can become difficult as a result of this.

SRMs have a wide speed range due to their durability, making them ideal for traction applications. Due to the varying operating conditions and limits that develop at different speeds, the control mechanism will change across this large speed range. The control for SRMs must be able to account for operating under these various situations, making controller design more complicated.

Because of these difficulties, SRM controls necessitate a certain level of sophistication and sensitivity on the designer's part. This chapter will provide a review of the basic principles of SRM control as well as a look at current control tactics. This chapter will also familiarise the reader with the most prevalent current control schemes in use, as well as more recent extensions to these strategies, such as the torque sharing function.

In order to develop a controller for any system, the designer must first have a thorough grasp of the system's dynamics. Controlling SRMs is no different. Understanding the dynamics of SRMs will help you appreciate the importance of various control measures that must be used in various situations.

3.2 System Dynamics:

The inherent dynamics of an SRM are modelled based on its magnetic characteristics due to its simple construction. The shape of the air gap defines the inductance profile, which affects the machine's dynamic behaviour, once the machine design is set. This inductance profile varies with location due to the doubly salient construction, which has a substantial impact on torque output. The rate of change of inductance affects torque production in SRMs. The following is the torque equation for linear operation conditions:

$$\tau = \frac{1}{2} i^2 \frac{\partial L(\theta)}{\partial \theta} \tag{3.1}$$

here L denotes phase inductance and θ denotes rotor position. The amount of torque produced scales with current, as seen in (3.1). However, as with any actual system, boosting current to the appropriate level takes a finite amount of time. The current behaviour can be compared to that of a first order electrical system since each phase of the machine can be reduced to an inductor with an iron core for analysis purposes. When a constant voltage, V, is supplied to the current, it behaves as follows: (3.2).

$$V = iR + L(\theta)\frac{\partial i}{\partial t} + i\frac{\partial L(\theta)}{\partial \theta}\omega_r \tag{3.2}$$

The motional electromotive force (EMF) created by the time-varying magnetic field caused by the phase current is represented by the last term on the right-hand side of (3.2). This voltage opposes the rate of change of current, which has an impact on the dynamic system's control capability. The induced voltage term, like the torque, is dependent on the rate of change of inductance, demonstrating the essential importance of machine inductance in the dynamics of the system, and indirectly, how much the machine design will affect the system's control constraints. The induced voltage term scales with rotational speed, as can be seen in (3.2).

3.3 Control Overview Of SRM:

Current control is at the heart of the SRM control scheme, in which the phase current is shaped based on a set of specified parameters to satisfy various speed, torque, power, and efficiency objectives throughout a wide variety of operating circumstances, according to the dynamics stated in (3.2). The torque-speed characteristics of the machine can be determined by having the ability to control the current. This enables for the creation of an outer closed loop in which the machine speed can be adjusted. Figure 3.1 depicts the traditional control paradigm utilised in SRMs in detail.

A current controller sends switching signals to the asymmetric bridge converter, which regulates the phase current depending on some current reference, $i_{ref,}$ at the heart of the control system depicted in Figure 3.1. The current reference, as well as other control factors such as conduction angles, are determined by the machine's torque and speed needs.

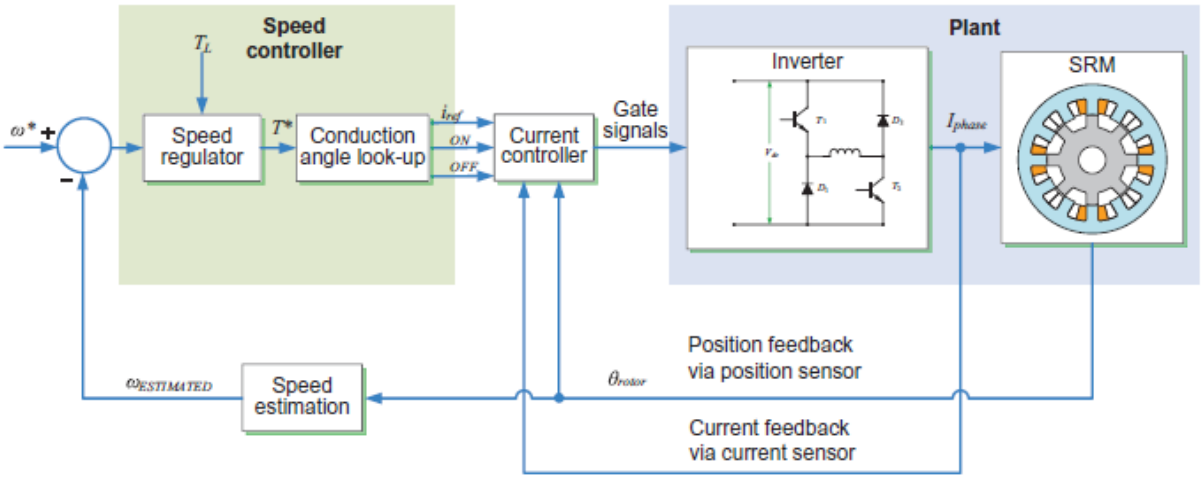

Figure 3.1 Control scheme for SRMs

Finally, by distinguishing the machine position θ_{rotor}, which is sensed using a position sensor, the machine speed, $\omega_{estimated}$. This is compared to the speed reference, $\omega*$ to estimate the required torque to accelerate or slow the machine in order to drive the load torque, T_L.

Parameters such as θ_{on} and θ_{off}, among many others, must be found through simulation in order to develop the whole control system depicted in Figure 3.1. The sections that follow provide a full description of each of the three controllers depicted in Figure 2.1, as well as the control parameters that are required.

3.4 Current Control:

3.4.1 Current Control scheme:

SRMs have a huge variance in inductance across their electrical cycle due to their distinctive construction, and hence their natural dynamics are very non-linear, as explained by (3.2). A motional EMF can be measured while the machine spins to quantify the rate of change of current in one phase of an SRM. This connection is described in (3.3).

$$\varepsilon = i\frac{\partial L(\theta)}{\partial \theta}\omega_r \tag{3.3}$$

The EMF can't be measured directly across the SRM's phase windings. The back EMF can be measured in a brushed direct current (DC) motor by rotating the armature in a continuous magnetic field with a prime mover and monitoring the voltage on the terminals. However, because the EMF

is also reliant on the phase current in the SRM, just turning the rotor will not generate any voltage. Only the phase voltage from the DC-link can be detected if the phase is excited. As a result, the motional EMF of the SRM differs significantly from the back EMF of a brushed DC motor. The motional EMF is induced in the phase as the motor rotates.

As a result, phase current increase is limited, and the motional EMF (generated voltage) is relevant to the topic of phase current dynamics in SRMs, as detailed in (3.4).

$$\frac{V-\varepsilon}{L}=\frac{\partial i}{\partial t} \tag{3.4}$$

By rearranging (3.2) and ignoring the effects of phase resistance, the relationships between the DC-link voltage, V, the motional EMF, and the rate of change of current are shown in (3.4). The rate of change of current is determined by the machine speed since the EMF is a linear function of rotor speed.

Figure 3.2 shows the dynamic current profiles for the three-phase SRM without any current control. Excitation occurs during the rising inductance portion of the electrical cycle, as shown in Figure 3.2a, and the dynamic current profile at three different speeds is shown in Figure 3.2b. The induced voltage profile that is responsible for the shape of the matching current profiles in Figure 3.2b is shown in Figure 3.2c. While the induced voltage cannot be measured directly, it can be measured by modelling the terminal voltage at various rotor points under continuous current excitation.

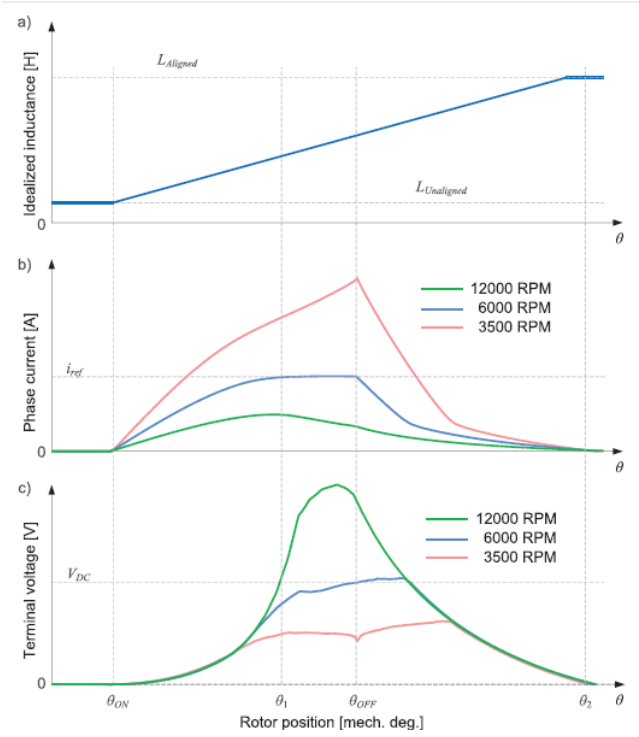

Figure 3.2 Dynamic profiles of phase inductance, phase current, and phase voltage at various operating speeds with constant conduction angles: (a) phase inductance, (b) phase current, and (c) phase voltage.

The terminal voltage at different rotor points under constant current excitation can be simulated to quantify voltage, which is not immediately quantifiable. The induced voltage profile in a dynamic profile like Figure 3.2c can be thought of as the voltage that the DC-link voltage must overcome to generate the current profiles seen in Figure 3.2b. Because this amount is a function of speed, as shown by equation (3.3), the induced voltage has a greater impact at higher speeds. Figure 3.2 shows that the phase is excited at θ_{on} and a positive DC-link voltage is applied across the phase windings at each speed.

Energy will be continuously injected into the phase upon turn-on, and the current will behave according to the dynamics stated in (3.2), until the phase is turned off and a negative DC-link voltage is supplied across it. When the phase is turned on, energy is withdrawn from it until the current is drained, which happens at θ_2.

Because the induced voltage has a low amplitude due to the low speed of operation at 3500 RPM, the current will continue to climb when the DC-link voltage is applied to the phase. The induced voltage does not limit the rate of change of current at this speed. Naturally, the high current will cause large copper losses, and if allowed unchecked, it will likely exceed the copper wires' thermal limit, causing damage to the coils. In practise, the converter chops this current so that it follows the current reference, $i_{ref,}$ in order to ensure torque production that meets the torque instruction. Trapezoidal current profiles result as a result of this.

The current automatically tapers down after the phase is excited at 6000 RPM because the induced voltage rises to the DC-link voltage value. Because the induced voltage's amplitude is near to the DC-link voltage, the current profile does not vary much until the turn-off time arrives.

The current profile when the machine is working at 12,000 RPM must be monitored in order to fully grasp the influence of the induced voltage. Even when a positive DC-link voltage is applied, the current spontaneously decays at 1 in this scenario. This is because, due to the fast speed, the induced phase voltage exceeds the DC-link voltage, causing the current to decrease, as illustrated in Figure 3.2c. Because of the influence of the induced voltage, which naturally limits the rate of change of current, controlling the peak value of current through switching may not be practicable at sufficiently high rates.

The conduction angles θ_{on} and θ_{off} are therefore controlled to generate the required average torque at high speeds. Due to the pulsated nature of the current profiles, however, torque quality will often suffer.

3.4.2 Hysteresis Control:

To prevent the current from exceeding the thermal limits and preserve smooth functioning of the machine, the peak current at low speeds must be managed to be at some prescribed value $i_{ref.}$ Switching the DC-link voltage that is delivered into the phase accomplishes this. The torque controller sets the current command, as indicated in Figure 3.1, and a current controller tracks it. The current controller provides switching signals, which are sent to the inverter to control the phase current and alter the DC-link voltage.

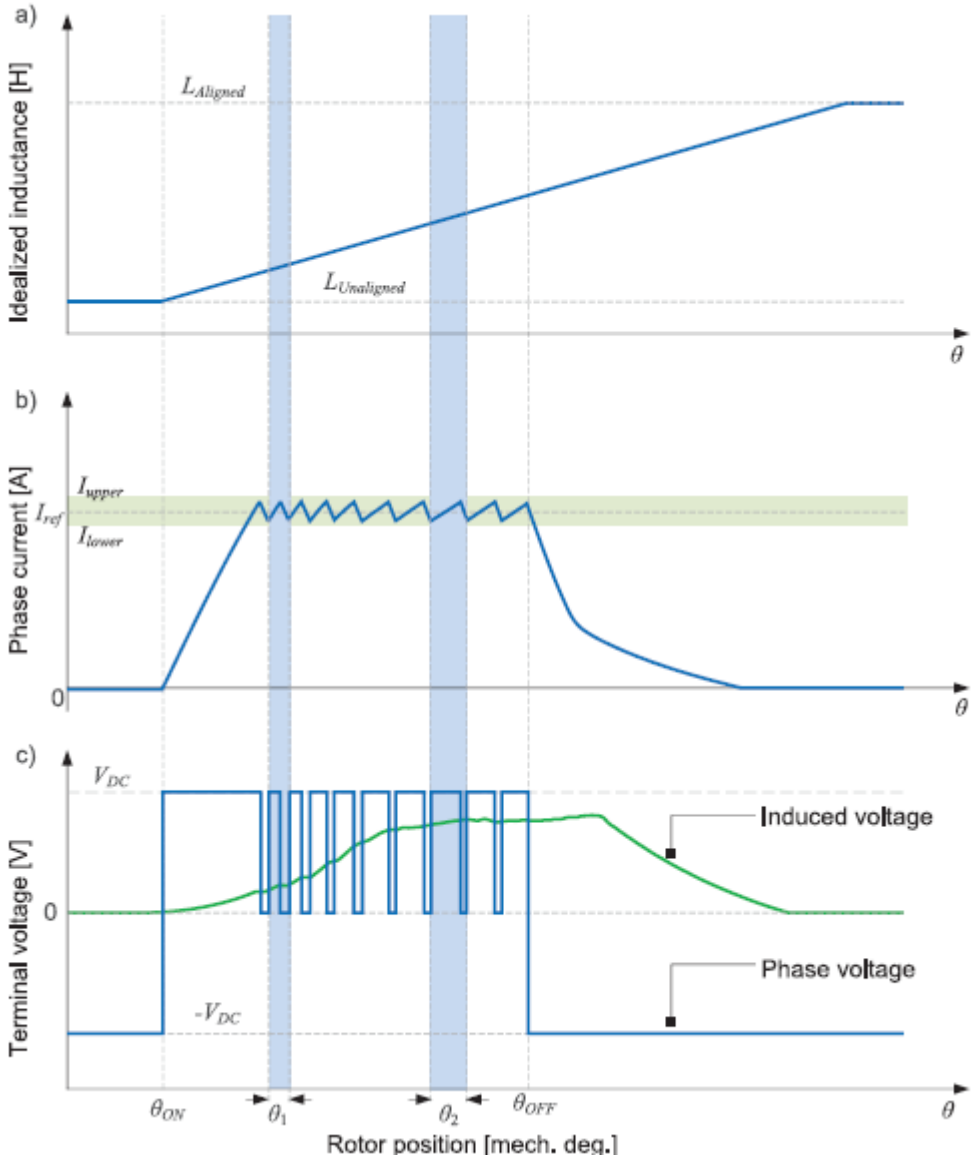

Figure 3.3 Current control for SRM with (a) phase inductance, (b) phase current, and (c) phase voltage displaying current chopping.

A hysteresis band is established by I_{upper} and I_{lower} to keep the phase current at a constant value $i_{ref.}$ As illustrated in, these values are derived using the current reference, $i_{ref.}$, and a tolerance β (3.5). In most cases, β is expressed as a percentage of the current reference (i_{ref}),

$$I_{upper} = i_{ref} \times (1+\beta)$$
$$I_{lower} = i_{ref} \times (1-\beta) \quad (3.5)$$

To limit the current amplitude to the level indicated by $i_{ref,}$ this hysteresis band is applied on the 3500 RPM current profile illustrated in Figure 3.2. Figure 3.3 depicts the resulting profile.

When comparing Figures 3.3 and 3.2, it can be seen that throughout the conduction period, Figure 3.3's voltage alternates between the DC-link voltage and zero to keep the current within the hysteresis band, thanks to feedback from the current sensor. The induced voltage amplitude stays below the DC-link value throughout the conduction period, necessitating current regulation at this speed.

The variable switching frequency of the hysteresis current controller is a function of the phase inductance as well as the width of the hysteresis band at any given time. Fundamentally, if the current rate of change is higher at a given instant, it will take less time for the current to travel beyond the hysteresis band, and the current controller will have to respond by switching the device faster. A lesser rate of change of current, on the other hand, means the switching will take longer.

As a result of the larger rate of change of current due to lower induced voltage and phase inductance near the unaligned location, the switching frequency will be higher.

As a result, the switching frequency will be affected by the choice of conduction period. The phase excitation begins closer to the unaligned location, as seen by the inductance profile in Figure 3.3a. The rate of change of current decreases as the induced voltage rises throughout the excitation period, therefore the switching period at θ_2 is substantially longer than the period at θ_1, as illustrated in Figure 3.3b.

To keep the current inside the hysteresis band, phase voltage can be varied between positive and negative DC-link voltage, or between zero and DC-link voltage, as shown in Figure 3.3c. While the former might result in a faster response, it would also necessitate a considerably higher switching frequency, resulting in larger current harmonics.

Furthermore, by reducing the size of the hysteresis band, current tracking and current ripple can be enhanced, as well as the torque ripple and acoustic aspects of the machine. The capabilities of the switching devices employed, the current sensor, and the motor controller, however, limit the breadth of this band that can be chosen. Finally, the conduction angles must be tuned, which has an impact on the motor's dynamic performance.

3.4.3 Impact of Stator Winding Conduction Angles:

The conduction angles θ_{on} and θ_{off} should be selected while developing SRM controls to maximise the motor's performance under varied operating situations. While hysteresis control will give the requisite torque at low speeds by selecting the appropriate current reference, torque quality and efficiency can be enhanced by carefully selecting the conduction angles. Meanwhile, because peak current control is not achievable at high speeds, conduction angles are the only characteristics that can be controlled. The effect of changing conduction angles on the dynamic current and torque profiles of an SRM is shown in Figure 3.4.

Three dynamic profiles with three sets of conduction angles are illustrated in Figure 3.4. Profile 1 uses a short conduction time, which uses less current and results in smaller copper losses. Due to the lack of commutation between phases, the short conduction duration results in low torque production and excessive torque ripple. In profiles 2 and 3, a longer conduction duration is used, and it can be observed in Figure 3.4c that the torque quality improves while the average torque increases.

However, by delaying the θ_{off}, some negative torque is produced, as indicated in Figure 3.4b by the phase torque. Because of the longer phase excitation duration, profile 3 has a later off than profile 2, resulting in more negative torque production. Despite the fact that both profiles 2 and 3 are turned off in the aligned position, tail current stays in phase due to the magnetic circuit's leftover stored energy.

Optimization is utilised in practise to discover the best conduction angles for each operational point on the torque speed map. When determining the ideal conduction angles, several conflicting objectives might be considered, as shown in Figure 3.4. The dynamics of the phase current, as well as the speed, are crucial considerations when choosing conduction angles. Due to the effect of increasing induced voltage, the rate of change of current decreases as the speed increases. As a result, the conduction angles have been advanced so that each phase has adequate time to energise before producing positive torque.

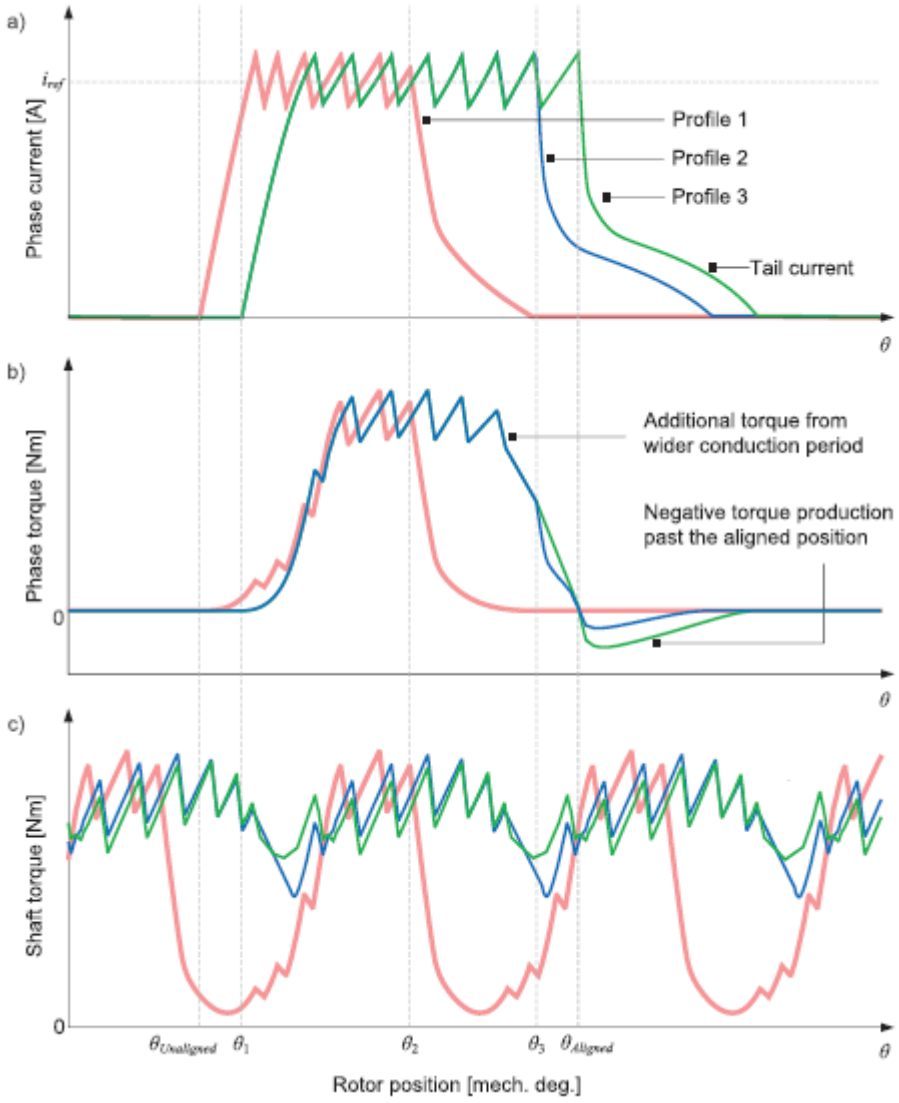

Figure 3.4 Variable conduction angles affect (a) phase current, (b) phase torque, and (c) shaft torque, as seen in dynamic profiles for SRM.

3.4.3.1 Optimization of conduction angles:

The choice of conduction angles has a big impact on the average torque and torque ripple. The impact of turn-on and turn-off angles on average torque, torque ripple, and other goals will be examined in this section. In multi-objective optimization, Teaching Learning Based Optimisation (TLBO) will be utilised to identify the optimal firing angles for SRMs. The words firing angles and commutation angles are used interchangeably in this work to refer to conduction angles.

The Teaching and learning based optimization technique were first introduced by Rao et al. This technique is inspired on the effect of the teacher on its student in a class. This technique somewhat copies the capability of teaching and learning of the teacher and capability of learners in a class. Therefore, the teacher and learner are the two basic aspects of this algorithm. This algorithm

primarily focuses on the two basic phases that is the teaching phase and the learning phase. Then the outcome for TLBO technique is considered in the form of result or grades attained by the learner which completely depends on the merits of teaching by the teacher. Furthermore, the learner also tries to learn through the interaction with other learners which may or may not improve the results of the learner itself.

TLBO technique is a population-based technique. In this technique the teacher will be providing the group of solution of a particular problem to the group of learners and the optimal results is considered to be solved by the teacher itself now the student has to perform the solution by themselves and if the solution of any student becomes better solution than the teacher itself then that solution will be considered as the best solution according to the greedy solution.

The flowchart utilized in the optimization issue is shown in Figure 3.5. It can be applied to specific operating locations as well as the complete operating range. The flowchart is divided into the four sections below. A specific SRM is described in the first section (I). It is possible to obtain and use the flux linkage and torque lookup tables in the SRM drive model. The flowchart then employs three loops. The optimizer calls the SRM drive model created in Simulink in the innermost loop (II). Variables supplied into the SRM drive include the turn-on, θ_{ON} and turn-off, θ_{OFF} angles. In different contexts, the objective functions utilized in the optimization problem varies.

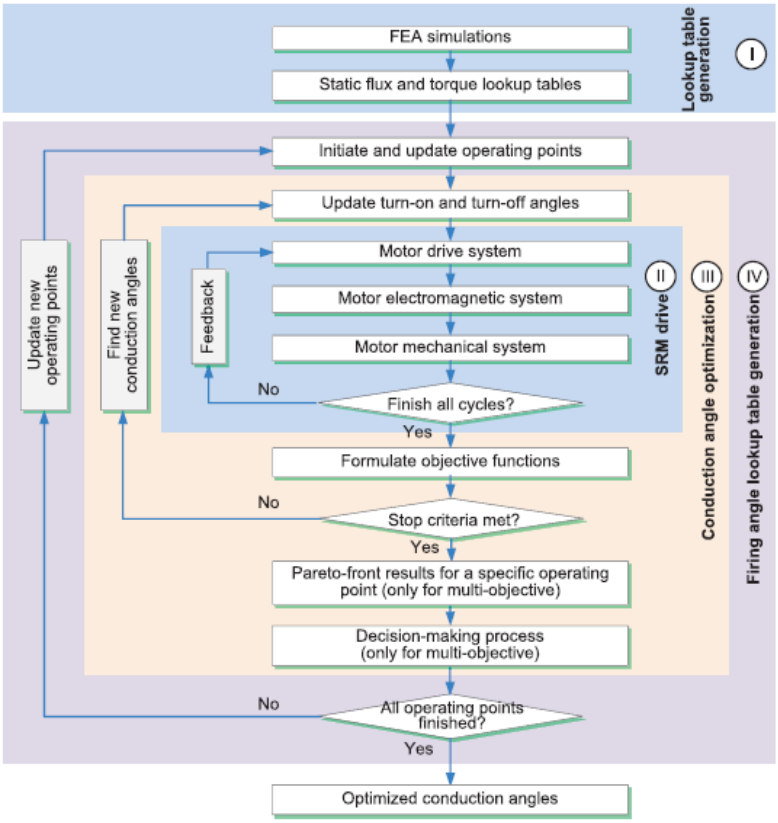

Figure 3.5 Flow-diagram for conduction angle optimization.

The optimizer continues its search for a global optimum in the second loop until the stop criterion limitations are met (III). If the problem is multi-objective, the optimal results for a single operational point are plotted in the Pareto-front, and decision-making logic is used to select a single front solution. The third loop (IV) feeds the second loop with either randomly or evenly selected operational points, such as reference speed and commanded current. Each operational point is associated with a single optimization problem.

3.5 Power Electronics Converter for SRM drive:

3.5.1 Asymmetric Bridge Converter:

The most often used converter in SRM drives is the asymmetric bridge converter for a three-phase SRM depicted in Figure 3.6. It provides for independent current regulation of distinct phases, resulting in excellent torque control. It does, however, include two switches and two diodes per phase, which is prohibitively expensive for low-cost applications.

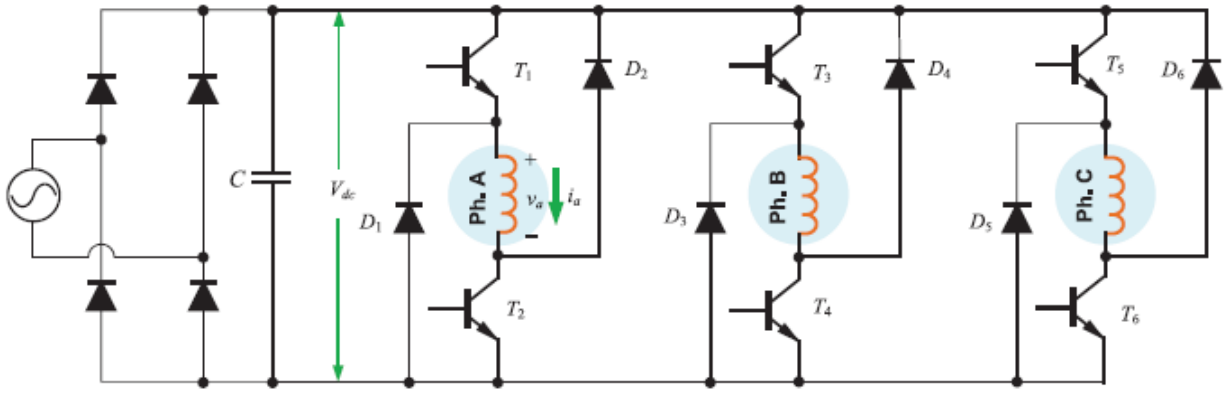

Figure 3.6 The asymmetric bridge converter for a three-phase SRM.

There are two switching patterns: bipolar modulation (hard switching) and unipolar modulation (soft switching). In hard switching, when the switches T_1 and T_2 are turned on, the phase voltage v_a is equal to the DC-link voltage Vdc, and the phase current i_a increases. When the phase current hits the upper limit of the current reference, the switches T_1 and T_2 are turned off. The phase current i_a circulates through the diodes D_1, D_2, and DC-link capacitors, and the stored energy in the magnetic circuit is transferred back to DC-link capacitors. In this condition, the phase voltage is equal to – Vdc and, therefore, the current decreases until it hits the lower limit of the hysteresis band. Then, the phase current i_a rises up again by turning on the switches T_1 and T_2. When the phase A current needs to be turned off completely, the switches T_1 and T_2 are both turned off. The phase current will decrease to zero until the stored energy in the winding is depleted. The operational waveforms are

shown in Figure 3.7. The required breakdown voltages of devices T_1, T_2, D_1, and D_2 should be higher than the DC-link voltage V_{dc}.

With the hard switching pattern, phase current circulates between the DC link and the phase winding in a switching cycle, which increases the power loss dissipation caused by switching losses as well as the current ripple in the DC-link capacitors. Soft switching can be applied to improve the converter's efficiency. The operational waveforms with soft switching are shown in Figure 3.8.

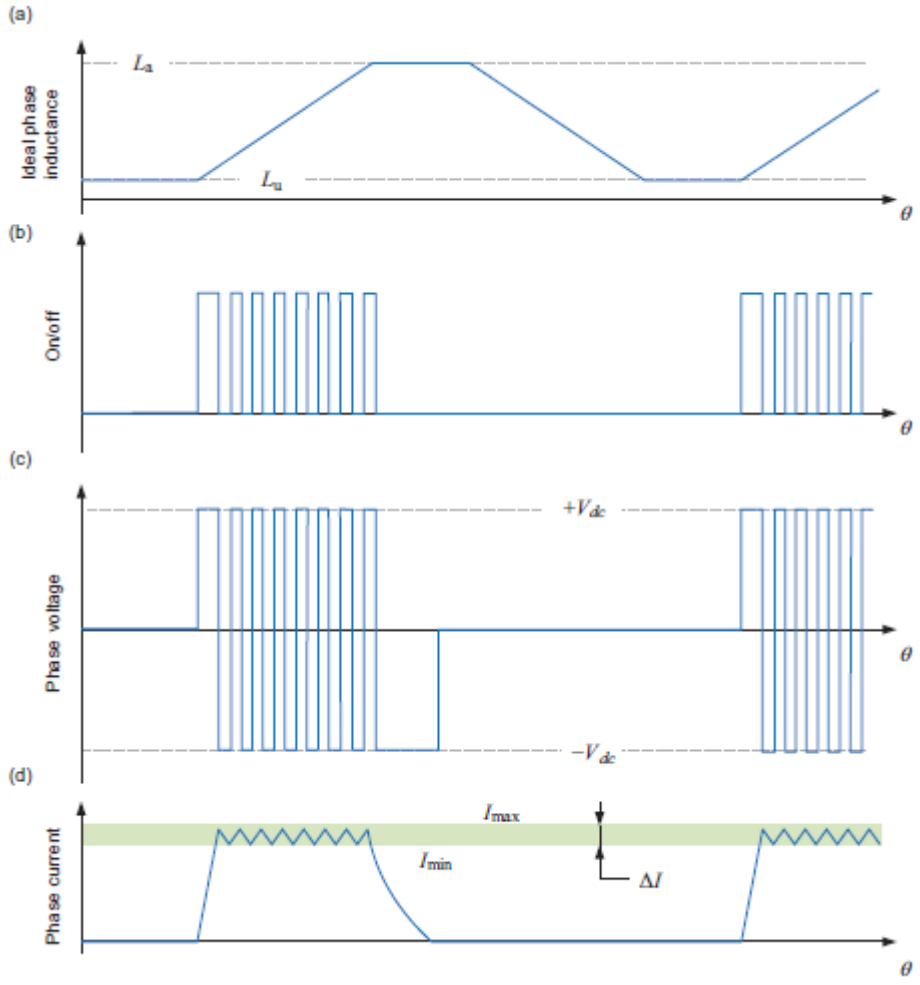

Figure 3.7 The operational waveforms of the asymmetric bridge converter using bipolar (hard) switching pattern: (a) ideal phase inductance, (b) on/off signal, (c) phase voltage, and (d) phase current.

During the interval θ_1 and θ_2, the switch T_1 is always on, and T_2 is turned on and off to track the current reference. When the switch T_2 is on, the phase voltage v_a is V_{dc}, and the phase current i_a rises. When i_a hits the upper limit of the current reference, the switch T_2 is turned off. Then, the phase current freewheels through the diode D_2 and the switch T_1. The phase winding voltage v_a is equal to the sum the voltage drops of D_2 and T_1 during conduction. Since the voltage drop is very low, the phase current i_a decreases slowly. After θ_2, the current reference becomes zero. Switches T_1

and T_2 are both turned off to reduce the phase current i_a rapidly. Compared to the hard switching shown in Figure 3.7, the switching losses are reduced with the soft switching.

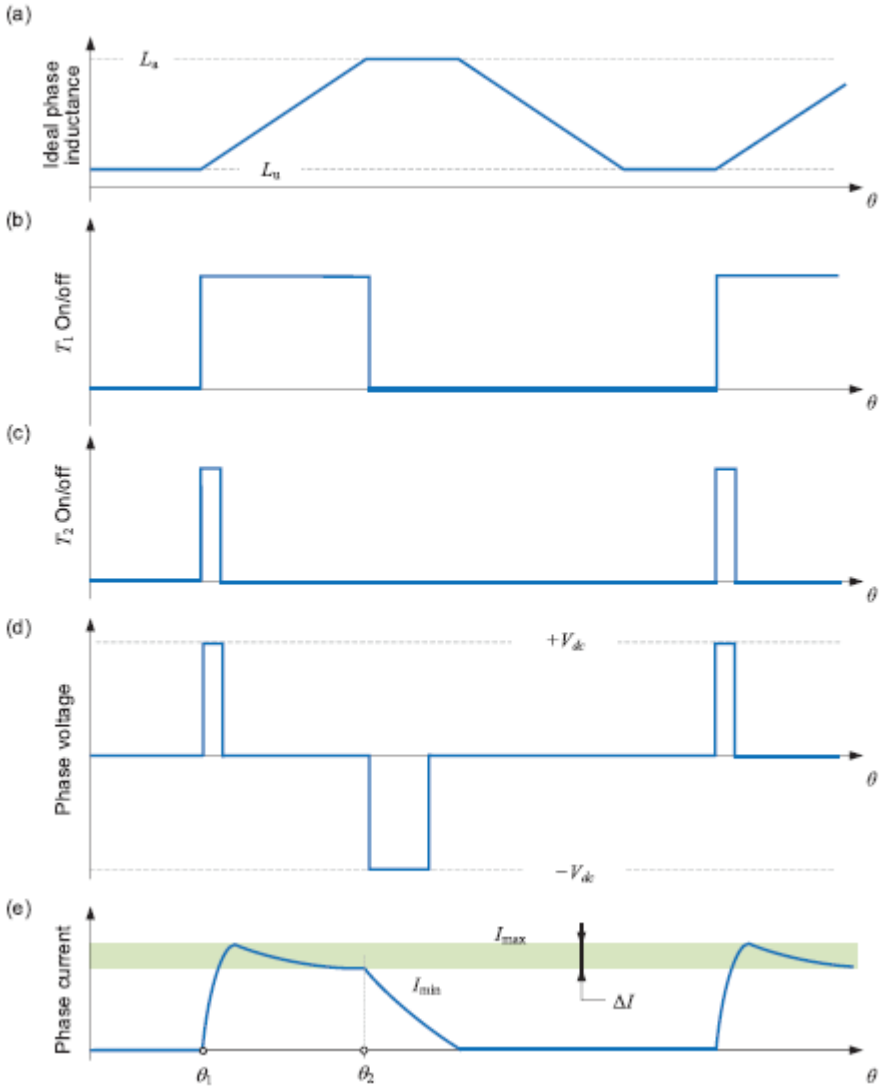

Figure 3.8 The operational waveforms of the asymmetric bridge converter using unipolar (soft) switching pattern: (a) ideal phase inductance, (b) T1 on/off, (c) T2 on/off, (d) phase voltage, and (e) phase current.

3.5.2 (N + 1)-Switch Converters:

In SRM drives, the phase winding does not conduct during the whole electrical cycle. Therefore, some of the power devices can be shared between different phase windings and the number of the switches can be reduced. Since the total number of switches in these topologies is one plus the number of phases, these converters are categorized as (N + 1)-switch converters. A (N + 1)-switch converter for a three-phase SRM is shown in Figure 3.9. Three-phase windings are connected to

four switches. The reduction of the number of switches is achieved by sharing a switch between two phase windings.

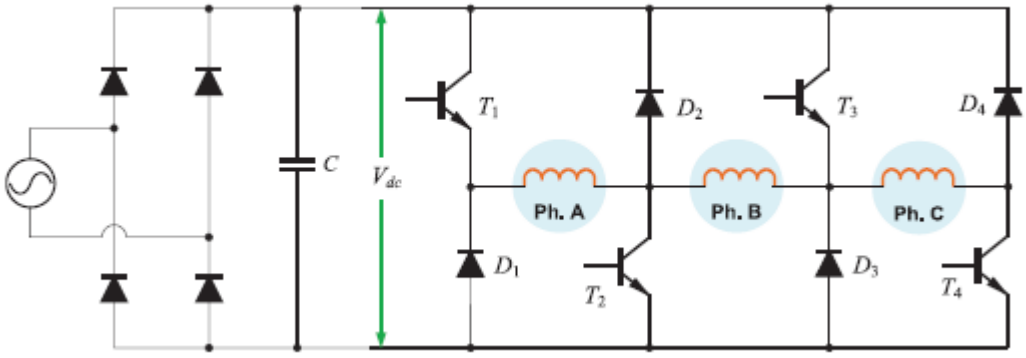

FIGURE 3.9 (N + 1)-switch converter for the three-phase SRM.

Compared to the asymmetric bridge converter, the current ratings of the shared devices (T_1, D_1, T_2, and D_2) increase. When SRM operates at low speed, the phase current can decrease rapidly because of the low induced voltage. Therefore, no overlapping between different phase currents occurs. The current of each phase can be independently controlled. However, when SRM operates at high speed, phase currents may overlap between different windings because of the higher induced voltage. This converter will lose the independent phase current control capability due to the shared power devices. For instance, when phase A is required to be turned off, both T_1 and T_2 should be off to decrease the phase current to zero. If phase *B* needs to be excited before phase A current falls to zero, T_2 and T_3 should be on. Therefore, there is a contradiction for the required switching status of T_2. In order to avoid the current overlap at high-speed operation, the conduction angle of phase *B* needs to be delayed during the commutation from phase *A* to phase *B*. By delaying the conduction angle, the generated torque is reduced. Therefore, the drawback of this converter is that it cannot independently control the phase currents, especially at high speed.

In order to improve the current control performance, a converter with shared devices for the four-phase SRM is shown in Figure 3.10. Compared to the (N + 1)-switch converter shown in Figure 3.9, there is one more switch and one more diode for this converter shown in Figure 3.10. The phase windings *A* and *B* share the power devices D_2 and T_2. The phase winding *C* and *D* share the power devices D_5 and T_5. As these devices are not shared by the adjacent phase windings, this converter can guarantee that only one phase current flows through each device anytime.

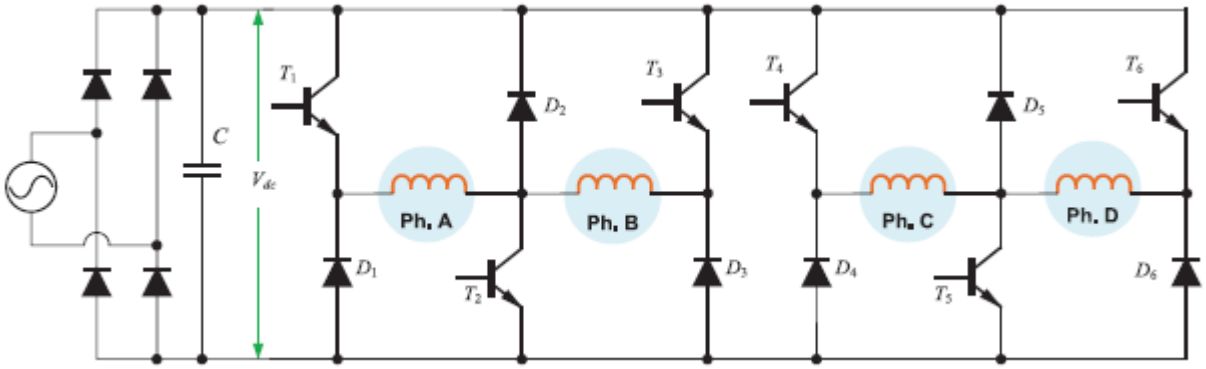

Figure 3.10 A converter with shared devices for the four-phase SRM.

Therefore, each phase current can be independently controlled. The torque control performance is better than that of the (N+1)-switch converter in Figure 3109. However, this converter is only suitable for the SRM with an even number of phases.

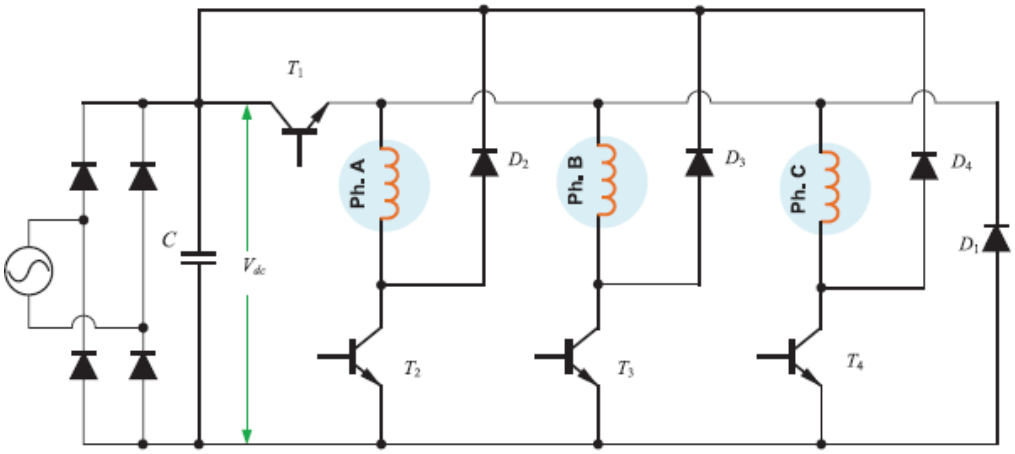

Figure 3.11 An alternative (N + 1)-switch converter for the three-phase SRM.

Another example of a (N+ 1)-switch converter for the three-phase SRM is shown in Figure 3.11. The switch T_1 and diode D_1 are shared by three-phase windings and, therefore, the current ratings of T_1 and D_1 are higher than other switches. Similar to the converter shown in Figure 3.8, the phase currents cannot be controlled independently when they overlap at high speed.

3.5.3 C-Dump Converter:

A C-dump converter is shown in Figure 3.12. This converter contains both the buck and boost converters. The operational waveforms of C-dump converter are shown in Figure 3.13, and the illustration of five modes of C-dump converter is depicted in Figure 3.14

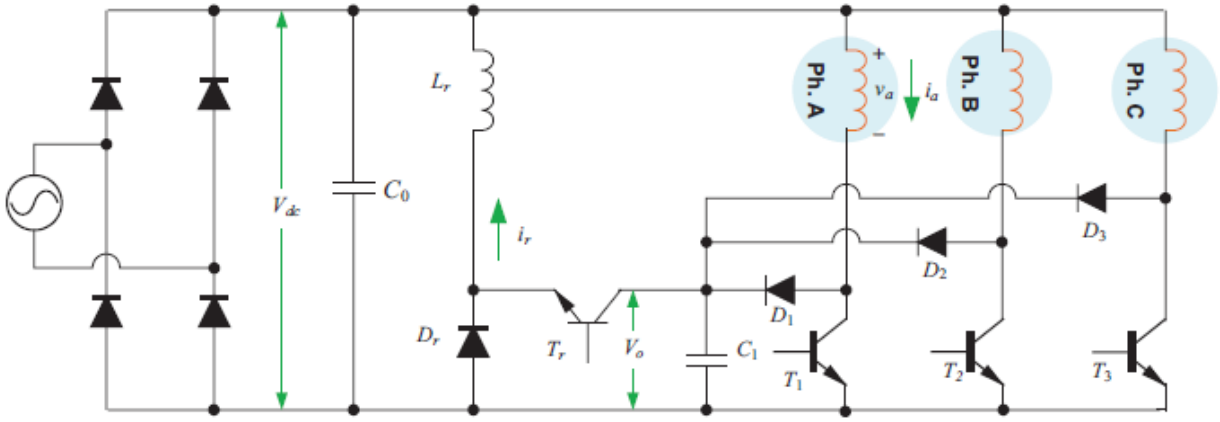

Figure 3.12 The conventional C-dump converter.

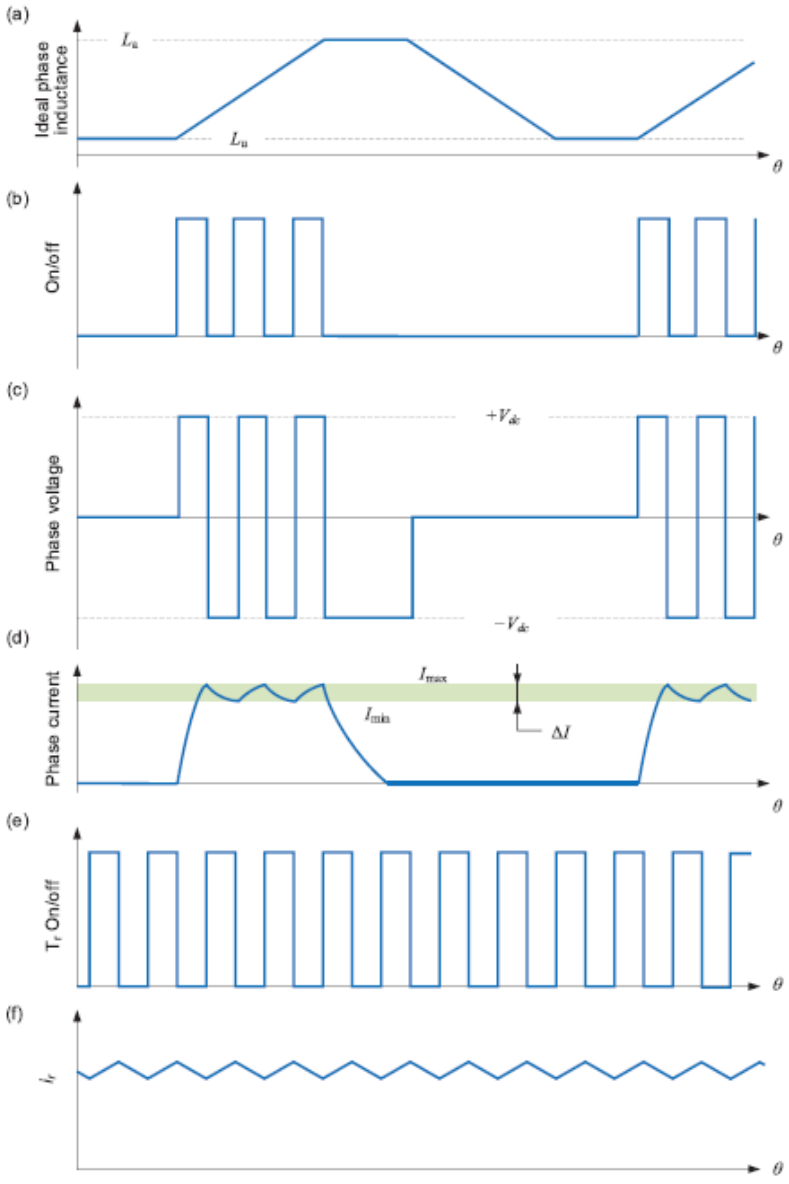

Figure 3.13 The operational waveforms of the conventional C-dump converter: (a) ideal phase inductance, (b) on/off, (c) phase voltage, (d) phase current, (e) Tr on/off, and (f)i_r

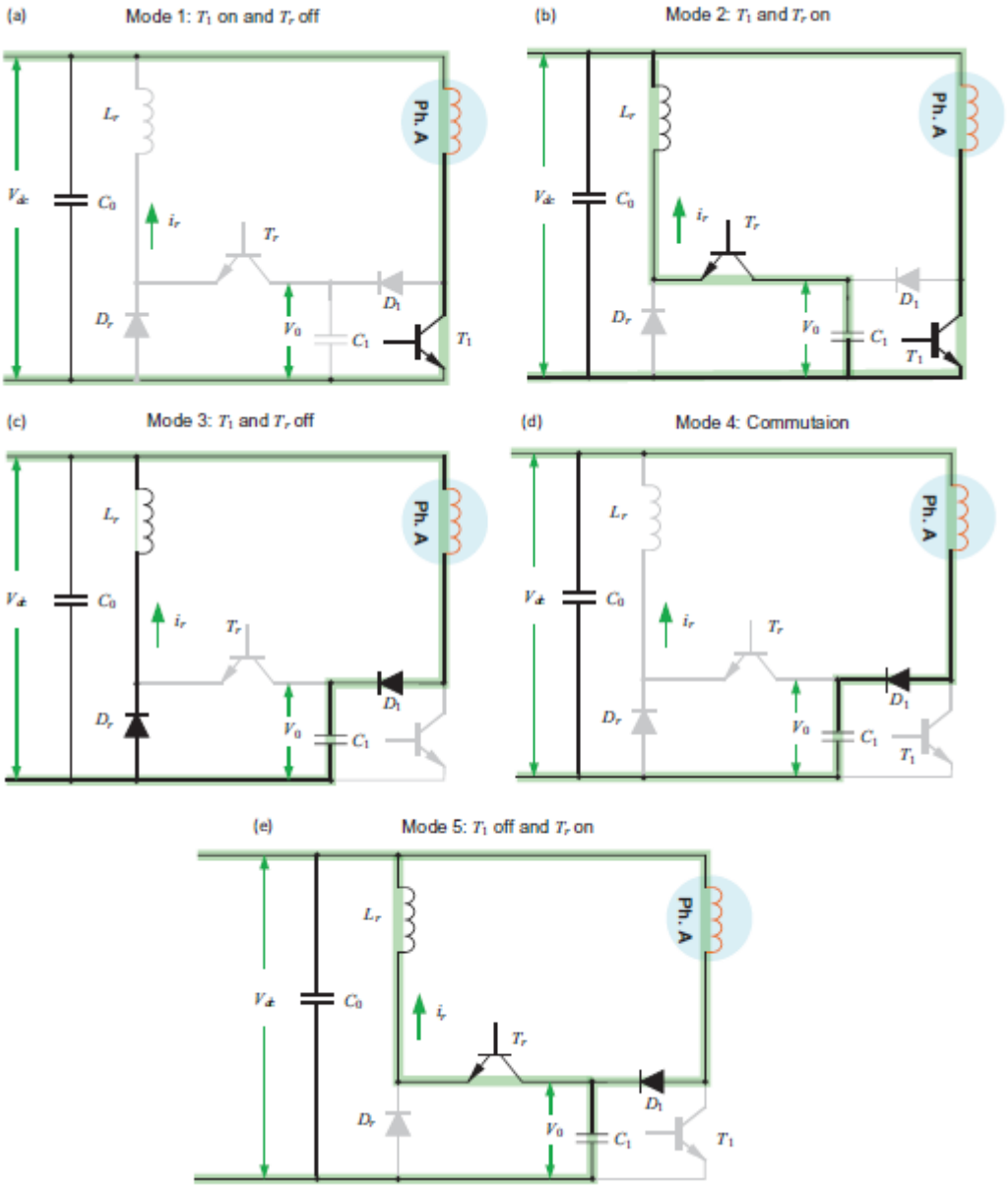

Figure 3.14 Five Modes of C-dump converter: (a) Mode 1, (b) Mode 2, (c) Mode 3, (d) Mode 4, and (e) Mode 5.

By taking phase A as an example, the DC-link voltage V_{dc}, the inductance of phase A winding, the switch T_1, the diode D_1, and the capacitor C_1 make up a boost converter. The capacitor C_1, the switch T_r, the diode D_r, the inductor L_r, and the DC-link voltage Vdc make up a buck converter. T_1 is used to control the phase current and Tr is used to control the voltage output of the capacitor C_1. When phase A current is below the reference, T_1 is turned on and V_{dc} is applied to the phase winding and phase A is working in mode 1 or 2. When the current of phase A rises above the reference, T_1 is turned off and $V_{dc} - V_0$ is applied to the phase winding. Phase A now works in one of the modes 3, 4, or 5, depending on V_0. Once the status of T_1 is defined by the phase current, the

specific operational mode can be utilized by the status of T_r. For example, when phase A current is below the reference and T_r is on, phase A is working in mode 2. When the current of phase B needs to be built up, T_2 is turned on and T_1 is turned off in Figure 3.12. The current of phase B flows through C_0 and T_2, and the phase A current flows through D_1, C_0, and C_1, and charges C_1. Thus, the C-dump converter allows independent control of different phases. T_r is used to control the voltage V_0 to provide higher demagnetization voltage during the commutation, leading to the higher voltage ratings for power devices. The additional inductor and switches/diodes are needed, which may increase the costs. Also, the C-Dump converter does not achieve freewheeling, which may increase the acoustic noise and switching losses.

3.5.4 N-Switch Converters:

Several converters with a single switch per phase are available. For an N-phase SRM, if the number of the switches of the converter is N, then these converters are categorized as N-switch converters. An N-switch converter using bifilar windings for the three-phase SRM is shown in Figure 3.15. The bifilar phase winding contains two closely spaced, parallel windings. For each phase, one of the bifilar windings is connected to a switch and the other one to a freewheeling diode.

The operational waveforms of this converter are shown in Figure 3.16. The voltage v_a is equal to the DC-link voltage V_{dc} when the switch T_1 is on, leading to an increase in i_a. The voltage across the D_1 is $(1 + n_1/n_2) * V_{dc}$ when T_1 is on, where n_1 and n_2 are the number of turns for the bifilar windings. When T_1 is off, the diode D_1 is forward biased. The voltage of the phase winding v_a is equal to $–(n1/n2) *Vdc$. Therefore, the phase current i_a decreases, and the stored energy of this winding is sent back to the DC link. The voltage across the switch T_1 is equal to $(1 + n1/n2) * V_{dc}$ when it is turned off. Although this converter has only one switch for each phase, the voltage ratings of power devices are higher compared to the asymmetric bridge converter.

Another single switch per phase converter with a split DC-link capacitor is shown in Figure 3.17. The operational waveforms are shown in Figure 3.18. When the switch T_1 is on, the phase voltage v_a is equal to $V_{dc}/2$ and, therefore, the phase current i_a increases.

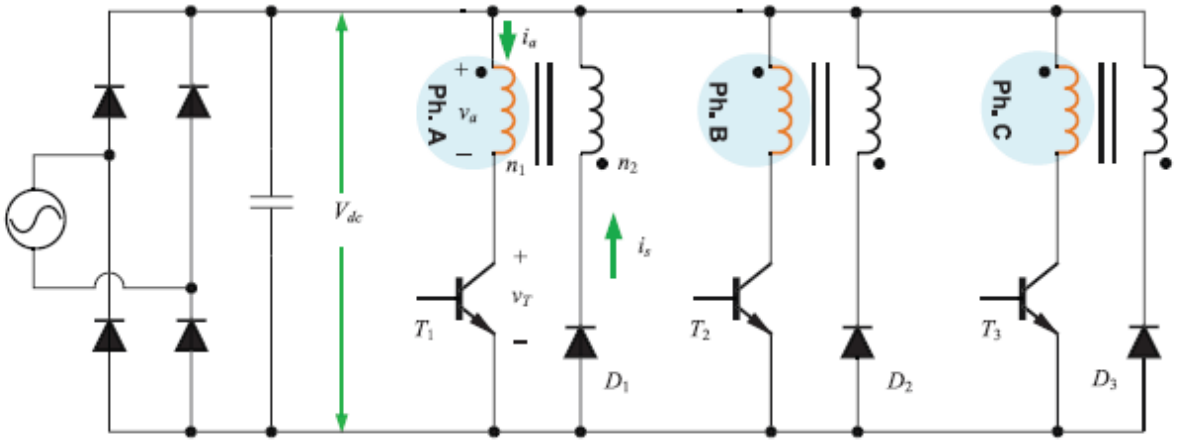

Figure 3.15 A converter with bifilar windings for three-phase SRM.

When the switch T_1 is off, the phase current ia freewheels through diode D_1, and the stored energy is sent back to the capacitor C_2. The breakdown voltages of the switch T_1 and the diode D_1 need to be higher than the DC-link voltage Vdc. It should be noted that the DC-link voltage utilization is low for this converter. Only half of the DC-link voltage can be applied to the phase windings. Although this converter only needs one switch for each phase, this advantage is outweighed by the low DC-link voltage utilization.

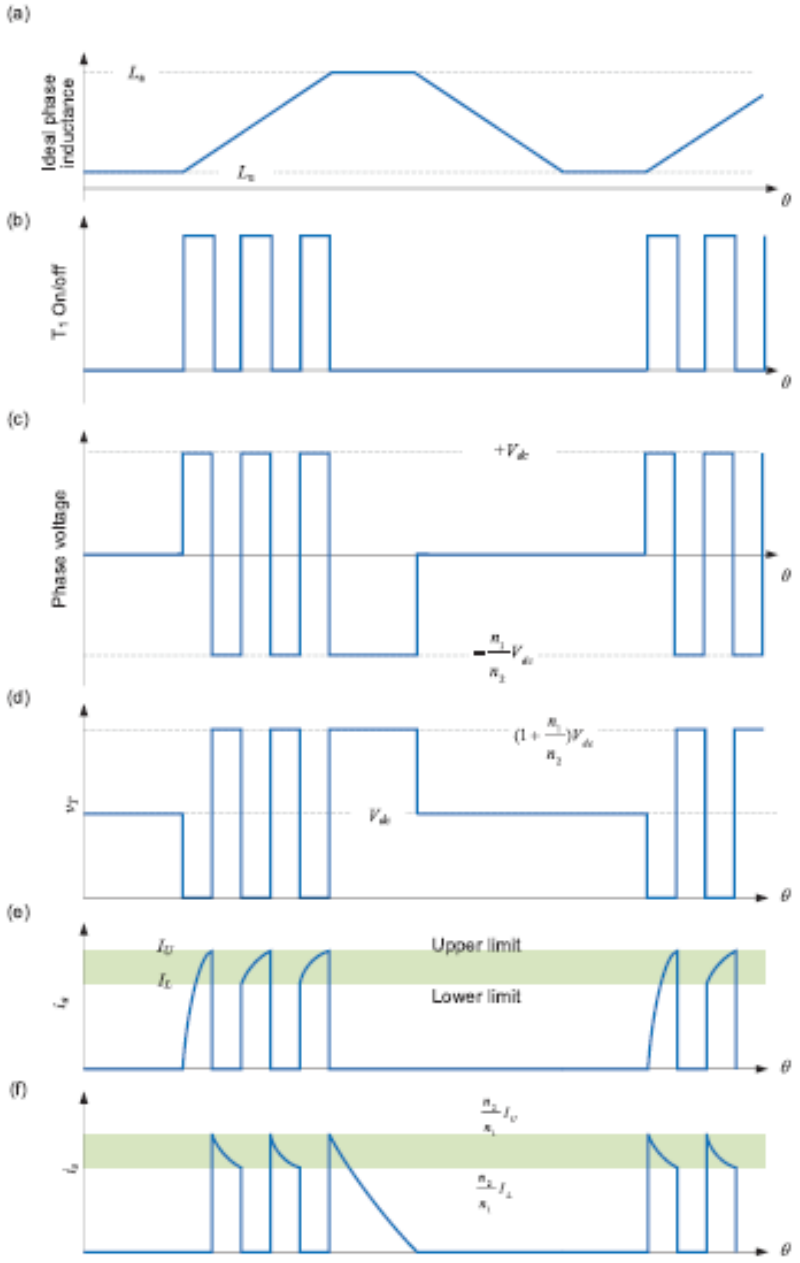

Figure 3.16 The operational waveforms of the converter with bifilar windings: (a) ideal phase inductance, (b) T_1 on/off, (c) phase voltage, (d) v_t, (e) i_a, and (f) i_s

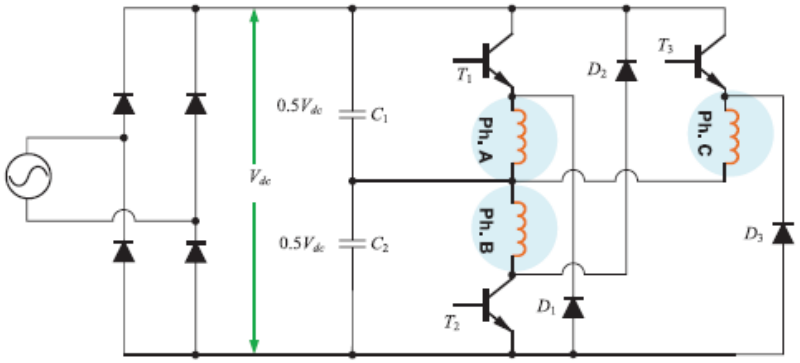

Figure 3.17 Split DC converter for three-phase SRM.

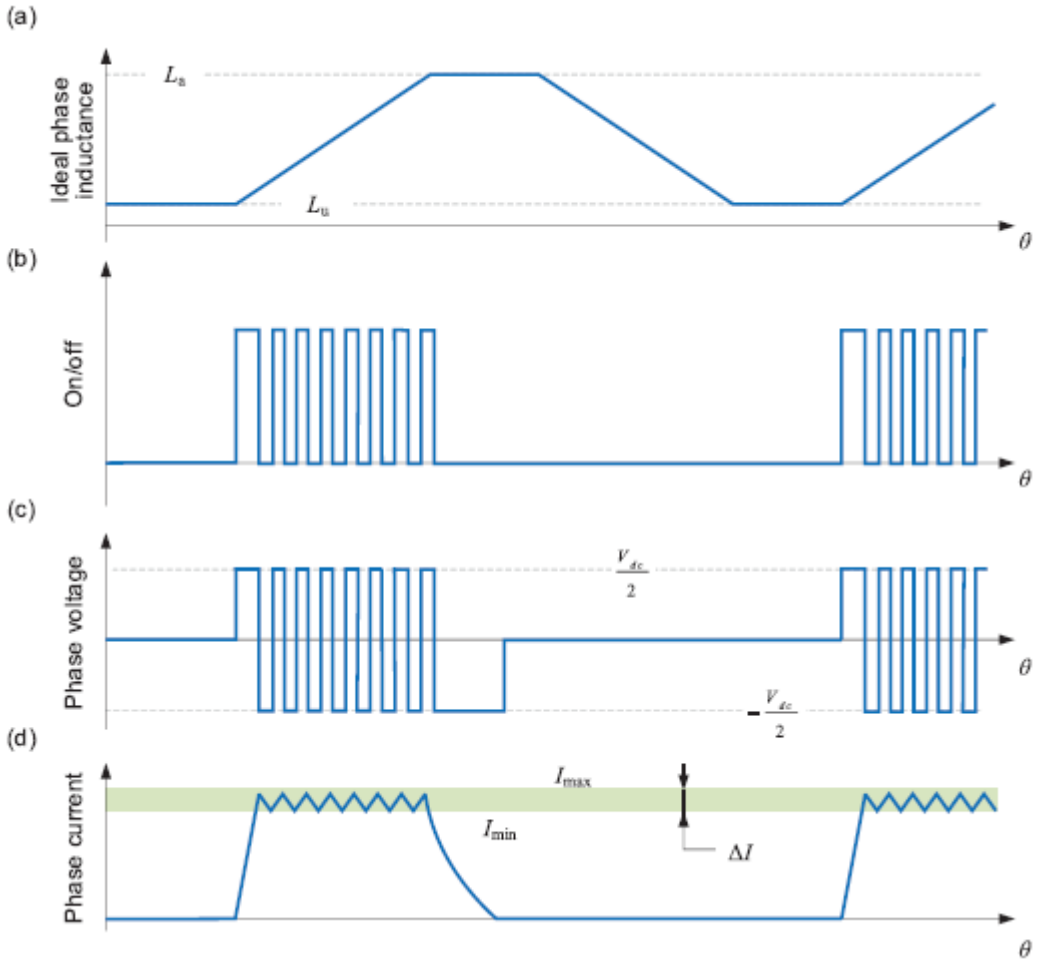

Figure 3.18 The operational waveforms of the split DC converter: (a) ideal phase inductance, (b) on/off, (c) phase voltage, and (d) phase current.

In order to improve the usable DC-link voltage for the phase windings, a split AC converter can be used as shown in Figure 3.19. A split AC converter has three switches, three diodes, and two capacitors. When the current of phase A is below the reference, T_1 is turned on and V_{dc} is applied. The phase A current flows through C_1 and T_1. When the current of phase A rises above the reference, T_1 is turned off and $-V_{dc}$ is applied. The current of phase A flows through D_1 and C_2. When the current of phase B needs to be built up, T_2 is turned on and T_1 is turned off. The current of phase B flows through C_2 and T_2. The demagnetization voltage of phase A is $-V_{dc}$. The split AC power converter also allows partial independent control of different phases. Compared with the split DC power converter, the split AC converter provides higher magnetization/demagnetization voltage, which decreases the commutation torque ripple. Moreover, no efforts have to be made to balance the voltage of C_1 and C_2. The usable voltage for the windings is the DC-link voltage V_{dc} in this converter. The power devices need to have a voltage rating two times the DC-link voltage.

An alternative single switch per phase converter is shown in Figure 3.19. When phase A needs to carry the current, the switches T_2 and T_3 are turned on and off. When phase B needs to carry the current, the switches T_1 and T_3 are operating. Because of the shared switch T_3 between phases A and B, the currents of these two phases cannot be controlled independently when the phase currents overlap. Similarly, the currents of phase C and phase D cannot be controlled independently. Also, the efficiency of this converter is lower as compared to the asymmetric bridge converter because of the extra diodes in series with the phase windings. Moreover, this converter is only suitable for the electric machines with an even number of phases. These drawbacks limit the applications of this converter.

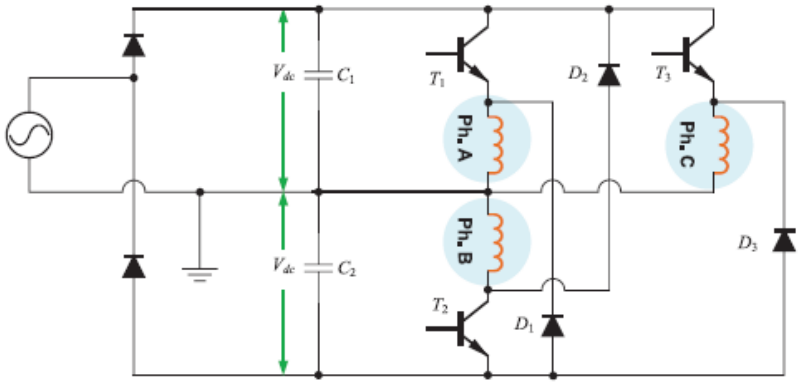

Figure 3.19 Split AC converter for three-phase SRM

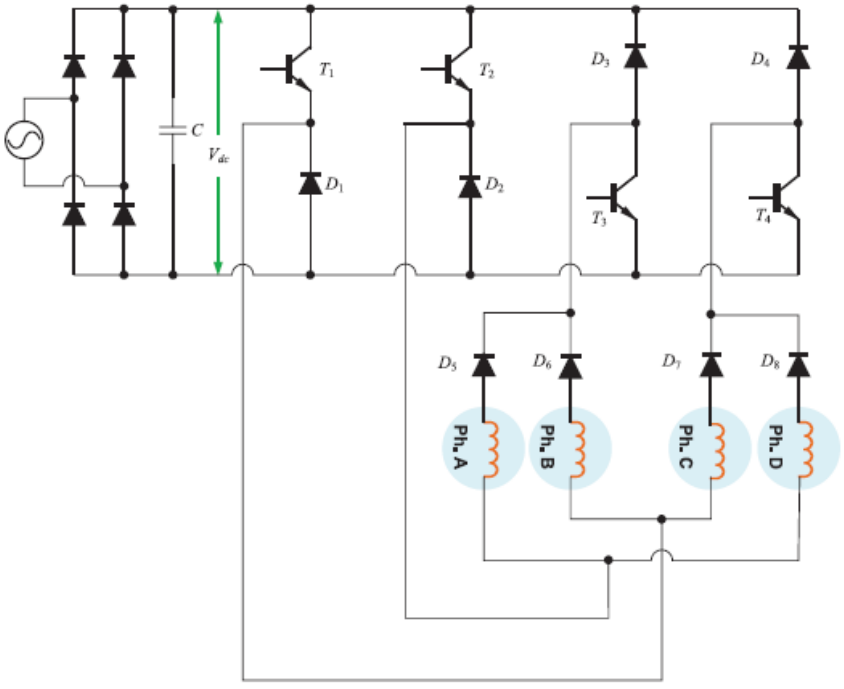

Figure 3.20 An alternative single switch per phase converter for a four-phase SRM.

CHAPTER 4: COMPOSITE SYSTEM MODEL

4.1 Introduction:

Switched Reluctance Machine works on the principle of varying magnetic reluctance. The rotor of the machine is pulled in any direction by varying the reluctance (clockwise or counterclockwise). The motor's torque is proportional to the square of the current magnitude, and hence is unaffected by the direction of current flow in the winding. Figure 4.1 depicts the relationship between Torque-Flux linkage and Rotor position as a block diagram.

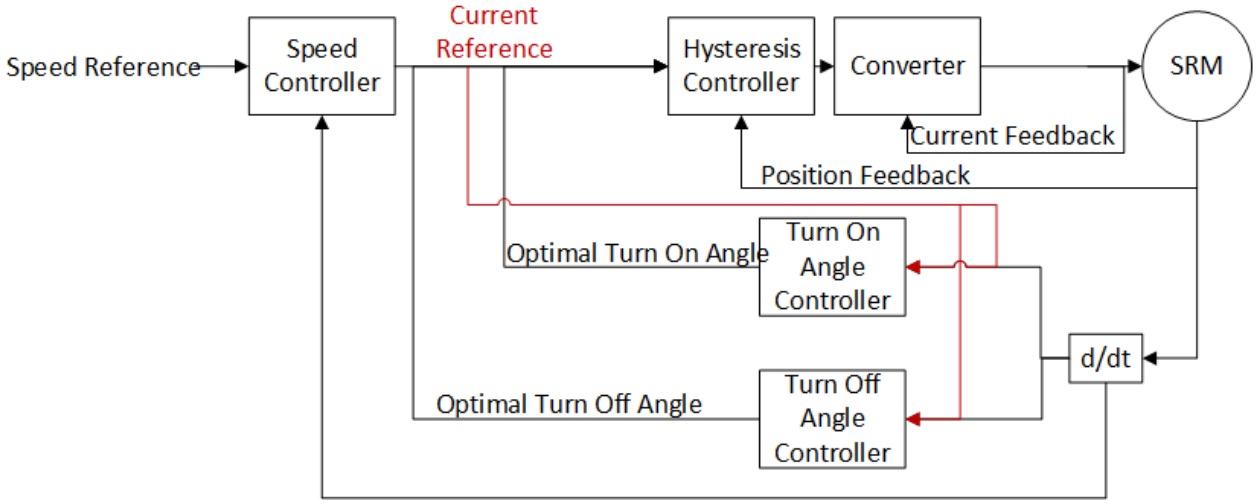

Figure 4.1 Block Diagram of SRM

4.1.1 Magnetic Characteristics:

Figure 4.2 shows the magnetic characteristics of a 60kW 6/4 SRM. The curve which does not saturate with respect to the current represents the unaligned inductance of the SRM while the curve which saturates with respect to the current represents the aligned inductance. The position where the pole faces of the rotor and stator align each other is taken as reference (0°).

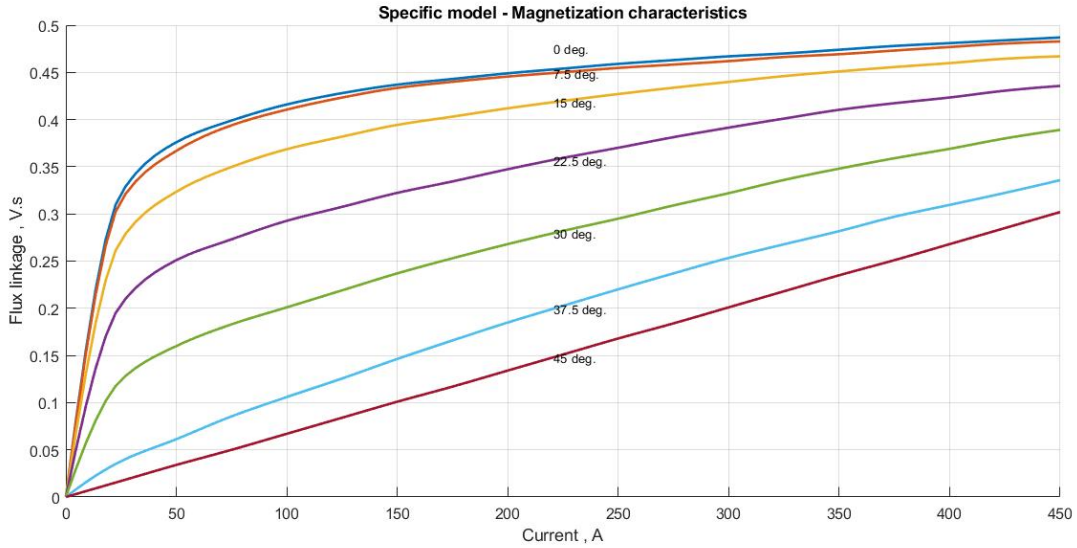

Figure 4.2 Magnetic Characteristics of 6/4, 60kW, SRM.

4.1.2 Teaching Learning Based Optimization (TLBO):

The TLBO technique was proposed in the year 2011 by Rao et al. [13]. TLBO is a meta heuristic method which primarily focuses on the two basic phases that is teaching phase and learning phase. Metaheuristic approaches, in general, produce a unique solution or group of solutions. Solution is basically the values of decision variable. Once the solution is generated, decision variables are sent to the optimization algorithm to evaluate the fitness function which is the only communication between the metaheuristic techniques and optimization problem for every solution. The evaluated fitness function value is returned to the algorithm. Thus, the algorithm sends the decision variables, and the problem sends back the fitness function. The algorithm uses intelligent operator to come up with a new set of decision variables which is again send to the algorithm problem and the fitness function value is received from the algorithm problem. This communication goes on repeatedly till a specified termination criteria is completed. Figure 4.3 shows the flow chart of the algorithm.

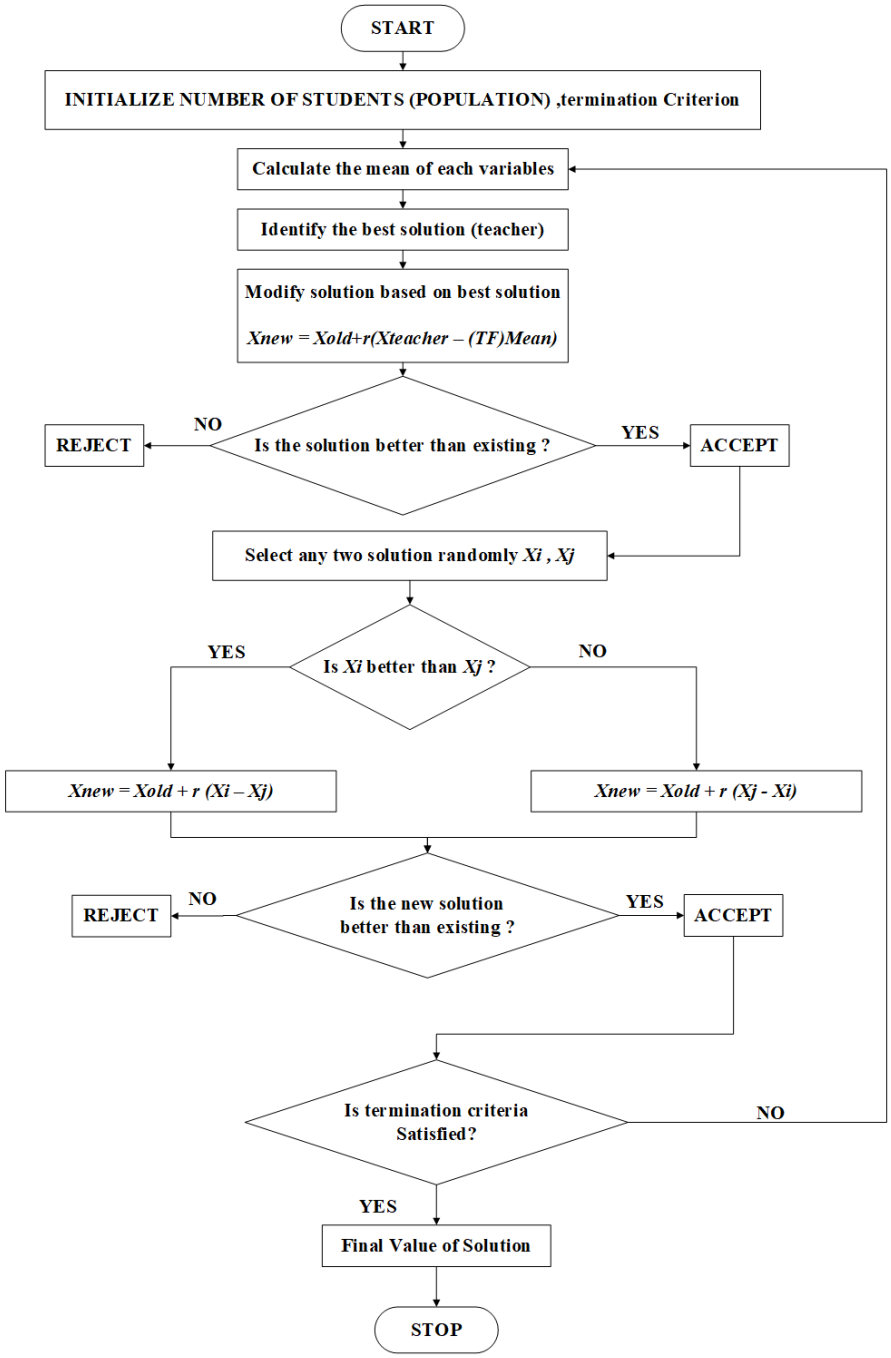

Figure 4.3 Flow Chart of TLBO algorithm

This thesis proposes a TLBO based technique to compute the turn-on and turn-off angles of the stator phase windings to optimize a multi objective function comprising the average torque, torque per unit copper loss and softness factor. Two real time controllers have been used to tune the turn-on and turn-off angles of the stator phase windings. The optimal turn on and turn off angles are used to generate the gate pulses for the converter switches. A hysteresis controller is also incorporated to regulate the stator current between prescribed limits. This thesis also presents an

application of the Indian Drive Cycle (IDC) in a SRM drive. In Indian roads, the Vehicle type is heterogeneous, including cyclists, mopeds, two and three wheelers, commercial transport, and buses etc. The Indian Drive Cycle (IDC), shown in Figure 4.4, was developed by the scientists at the Automotive Research Association of India, Pune in 1985 after collecting real world data from major cities representing actual driving pattern. Simulations are carried out to optimise a multi-objective function comprising the SRM drive performance indices like average torque, stator copper losses and the integral squared error of the motor and reference speeds. It is observed that the motor satisfactorily tracks the drive cycle speed while optimizing the drive performance indices. Simulation results validate the effectiveness of the proposed technique.

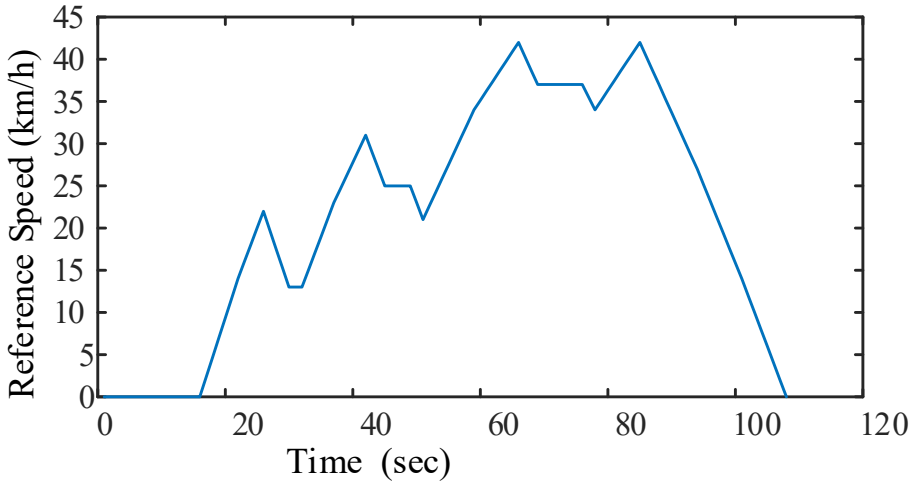

Figure 4.4: Indian Drive Cycle

CHAPTER 5: CASE STUDY AND RESULTS

5.1 Case Study 1:

A 6/4 SRM drive system is used for case study whose specifications are given in Table 1. A block diagram of simulation model is shown in Figure 5.1. The entire model was developed in SIMULINK. The desirable conditions for SRM drive systems are low output torque ripple, high average torque, and low copper losses. The decision variables are turn-on and turn-off angles of the stator phase windings. After every iteration, the torque per unit copper loss, ripple factor and average torque are optimized using the TLBO technique. The objective function to be maximized is given below,

$$F_{obj} = W_1 TC + W_2 T_{AVG} + W_3 SF \tag{5.1}$$

Where W_1, W_2, W_3 are the weighting coefficients.

In this paper, they were selected as 0.2, 0.6 and 0.2, respectively.

also

TC = Torque per unit copper losses

T_{AVG} = Average Torque

SF= Softness Factor = $\frac{\text{Average Torque}}{\text{Tmax} - \text{Tmin}}$

The SRM specifications along with the simulation parameters are shown in Table 1

Table 1: SRM Specifications And Simulation Parameters

Power rating	60kW
Rated speed	15000rpm
Input Voltage	650 V dc
J (Rotor Moment of Inertia)	0.069 kg-m^2
R_a	0.01 Ω

Table 2 : Optimization Parameters

Population Size	No. of Iterations	Decision Variable	
	50	**Turn On Angle**	**Turn Off Angle**
		LB = 35°	LB = 65°
		UB = 55°	UB = 85°

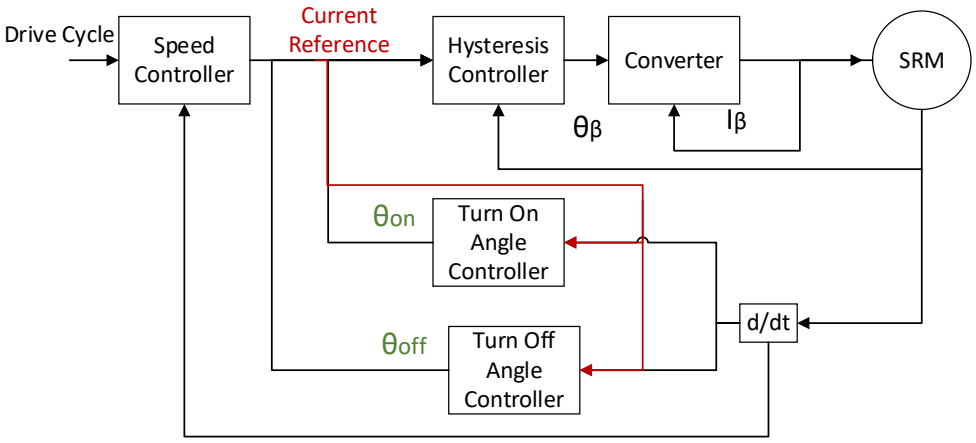

Figure 5.1 Simulation model

5.1.2 Results:

Table 2 depicts the parameters used in optimization. Turn-on and Turn-off angles of the stator phase windings are taken as decision variables with upper and lower bounds as shown in Table 2. The number of iterations is restricted to 50. Figure 5.2 shows the results of the optimization process with the objective function settling at a constant value of 60. Figure 5.3 shows the variation of the softness factor with time in seconds. It is observed that the softness factor with TLBO based controller has a higher value (lower torque ripple) than that without it. Figure 5.4 shows the variation of the average torque of the SRM drive with time. It is observed that the average torque with TLBO based controller is higher than that without it. Figure 5.5 shows the variation of the torque per unit copper loss of the SRM with time. It is observed that the torque per unit copper loss with the TLBO based controller is higher than that without it. Its high value indicates the efficiency of the drive. Figure 5.6 depicts the optimal value of the turn-off angle at 81° while Figure 5.7 shows the optimal value of the turn-on angle at 36°. Thus, for optimal drive performance of the given

SRM specification, the turn-off and turn-on angles should be 81° and 36° respectively. Figure 5.8 shows the plot of the stator current vs. time (in seconds.) It is observed from Figure 5.8 that the stator current is limited to 200 A by the hysteresis current controller. Figures 5.9 and 5.10 show the motor rpm and the developed Electromagnetic Torque (T_e) of the motor in Nm versus time.

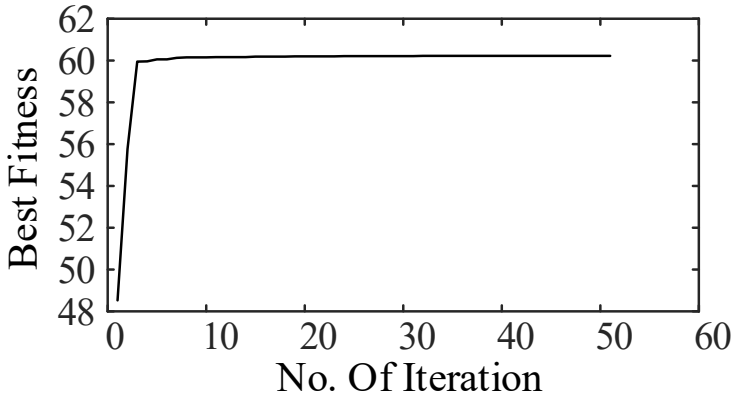

Figure 5.2 Optimization Curve

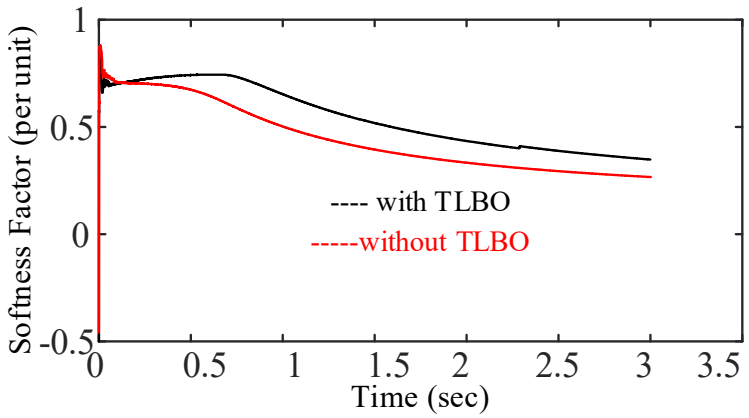

Figure 5.3: Softness Factor

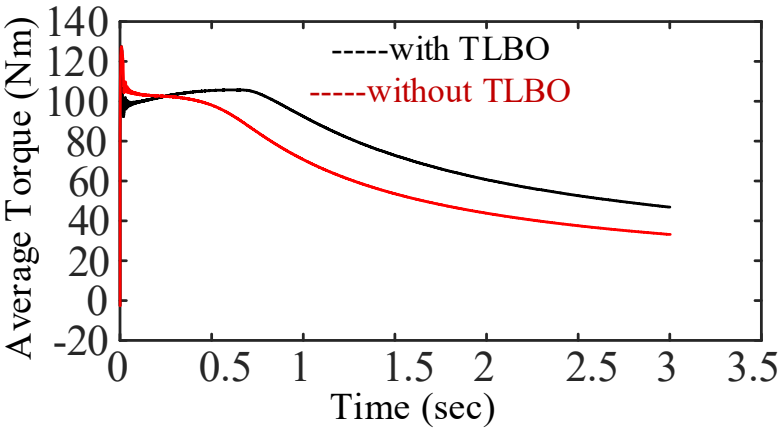

Figure 5.4: Average Torque

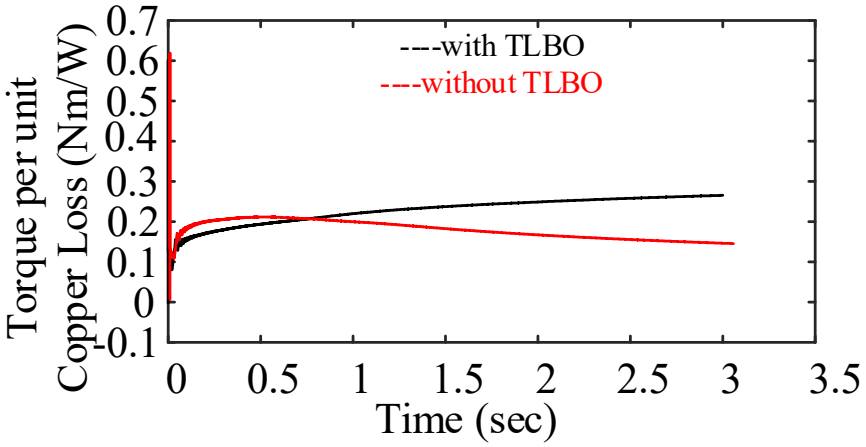

Figure 5.5: Torque Per Unit Copper Loss

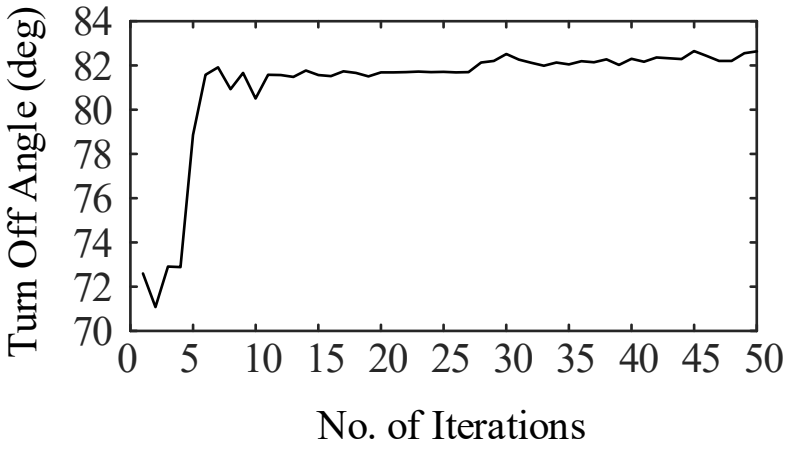

Figure 5.6: Turn Off Angle (deg) of Stator Winding

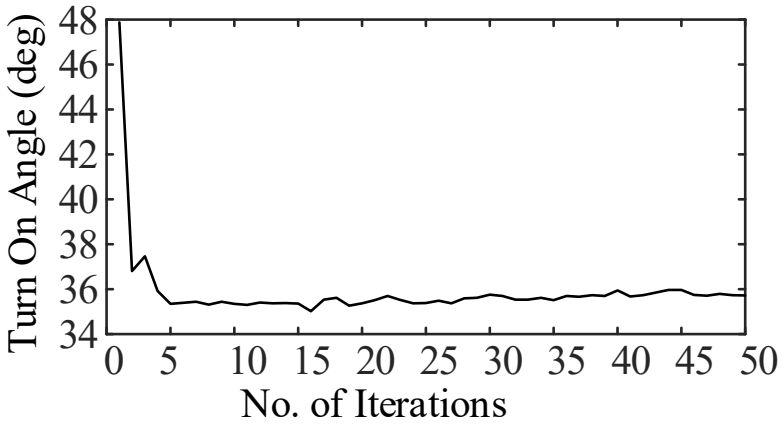

Figure 5.7: Turn on Angle (deg) of Stator Winding

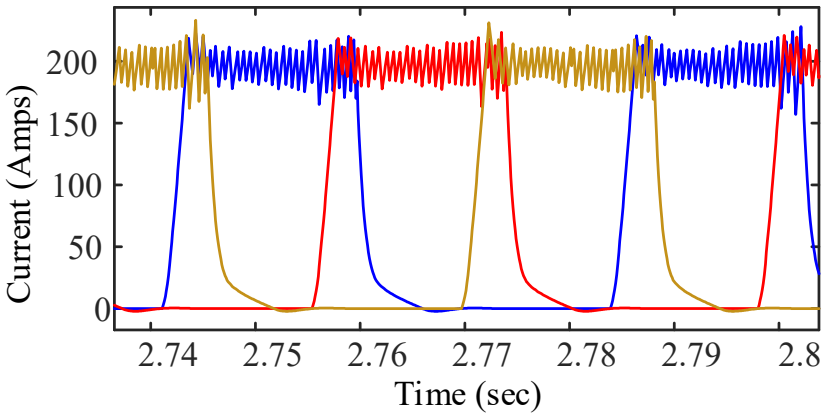

Figure 5.8 Stator current

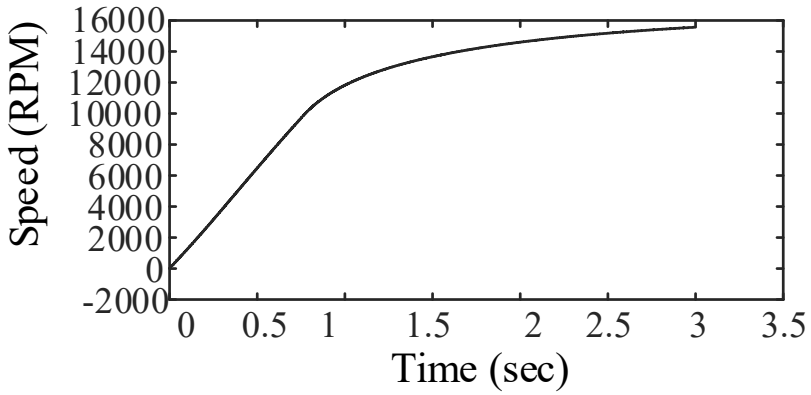

Figure 5.9: Speed (RPM)

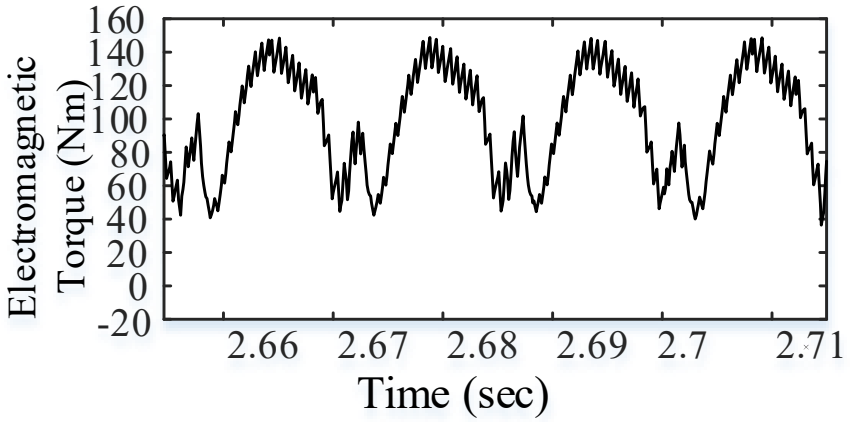

Figure 5.10: Electromagnetic torque developed by motor

5.2 Case Study 2:

Same motor configuration and optimization parameters as stated above in Table 1 and Table 2 respectively are used to perform another optimization problem. The desirable conditions for SRM

drive systems are low stator copper losses, high average torque, and low integral squared speed error. The decision variables are the turn-on and turn-off angles of the stator phase windings. After every iteration, the stator copper losses, integral squared error, and average torque are optimized using the TLBO technique. The objective function to be maximized is given below,

$$Fobj = W_1 / loss + W_2 T_{AVG} + W_3 / error \quad (5.2)$$

Where W_1, W_2, W_3 are the weighting coefficients.
In this paper, they were selected as 0.3, 0.4 and 0.3 respectively.

where
loss: stator copper losses
T_{AVG}: Average Torque
error: ($\int \varepsilon^2 dt$).

$$\varepsilon = \frac{\text{Motor Speed} - \text{Reference Speed}}{\text{Reference Speed}}$$

5.2.1 Results:

The turn-on and turn-off angles of the stator phase windings are taken as decision variables with upper and lower bounds as shown in Table 2. The number of iterations is restricted to 50. A tuned PI controller is used to control the motor speed. Figure 5.11 shows that the SRM tracks the drive cycle speed satisfactorily. The optimal turn-on and turn-off angles of the stator phase windings for different speeds are shown in Figure 5.12(a) and (b). It is observed that turn-on angle lies between 40° and 50° whereas the turn-off angle lies between 70° and 85°.Figure 5.13 shows the copper losses in the stator phase windings of the SRM. Losses play a vital role in determining the efficiency of motor. To achieve high speed and maneuverability, the losses in the machine should be kept minimum. Figure 5.14 shows the Integral Squared Error (ISE) at every data point over the drive cycle. The PI controller is tuned such that the rise time is minimum, and the speed error is low. Figure 5.15 shows the optimum average torque developed on the motor shaft over the entire drive cycle. It is observed that the average torque spans 10 Nm under no load condition. Figure 5.16 (a) and (b) shows the winidng currents at 21 km/h and 42km/h motor speed, respectively. It is observed that the current remains below 20 A in both the conditions because of the current controller. Figure 5.17 (a) and (b) shows the electromagnetic torque developed in the motor at 21 km/h and 42 km/h motor speed respectively.

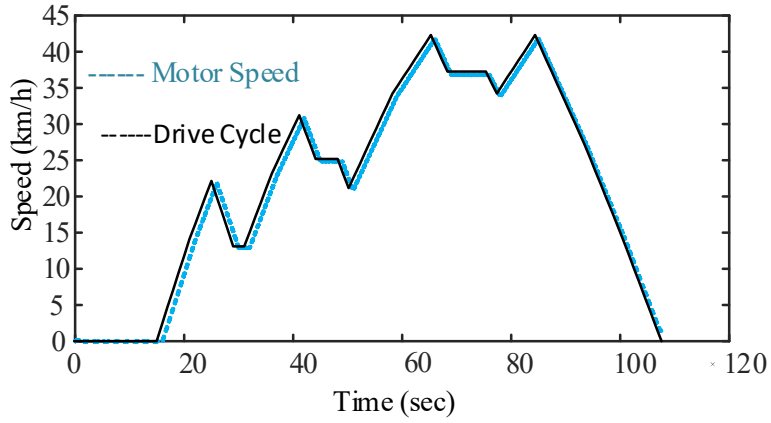

Figure 5.11: Motor and IDC speed variation

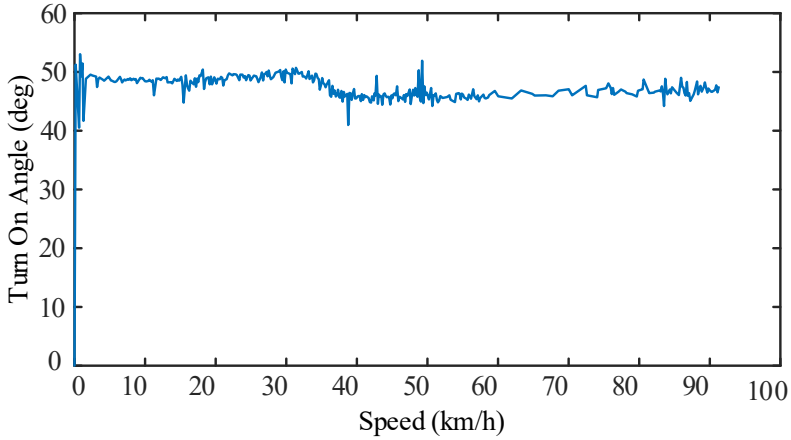

Figure 5.12(a): Variation of turn-on angle with IDC speed

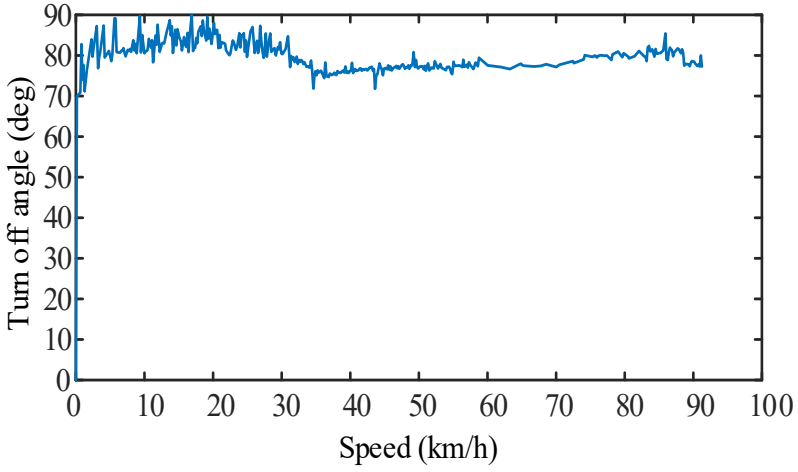

Figure 5.12(b): Variation of turn-on angle with IDC speed

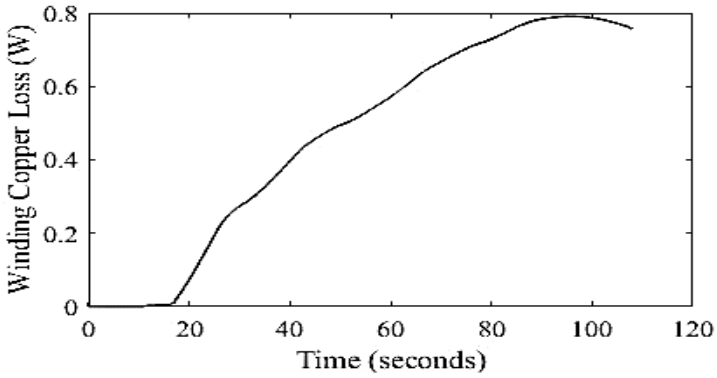

Figure 5.13: Variation of winding copper losses with time

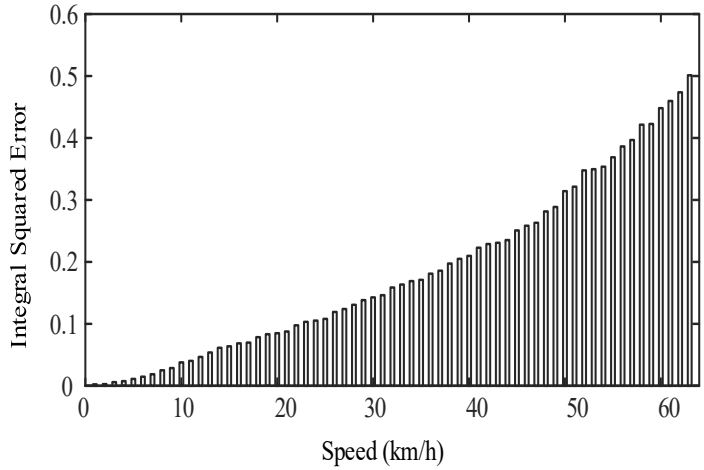

Figure 5.14*:* Integral Squared Error (ISE) variation with IDC speed

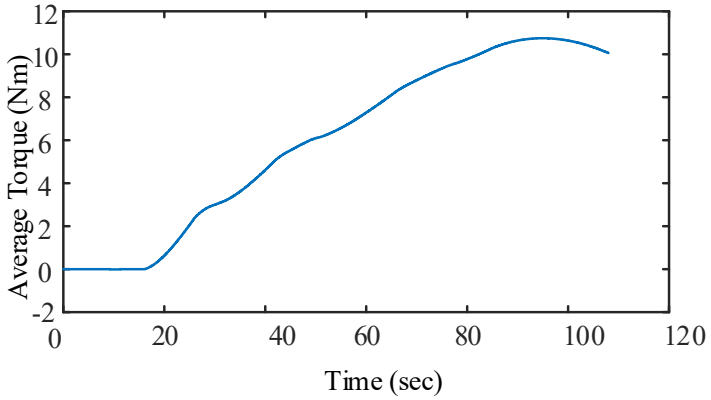

Figure 5.15: Optimal Average Torque

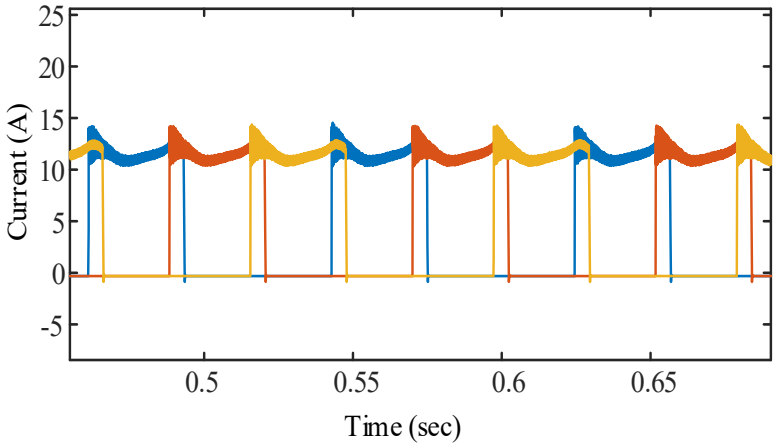

Figure 5.16(a): Stator current variation with time at 21 kmph

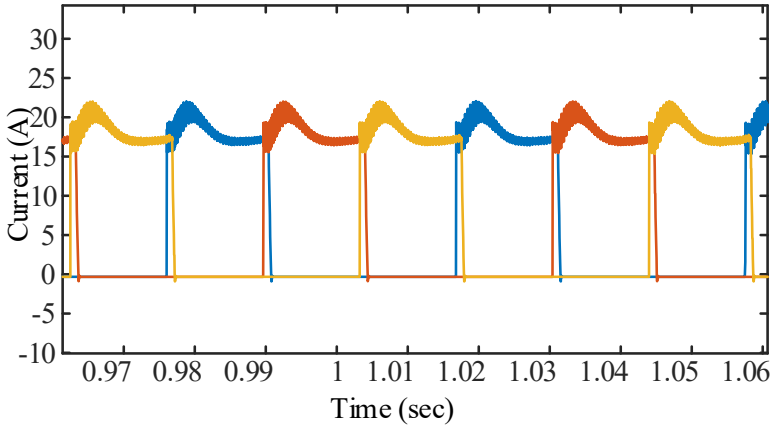

Figure 5.16(b): Stator current variation with time at 21 kmph

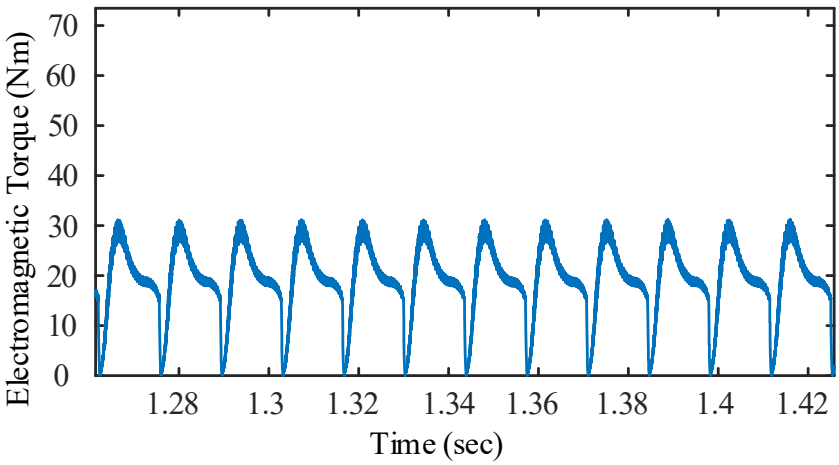

Figure 5.17(a): Variation of electromagnetic torque with time at 21 kmph

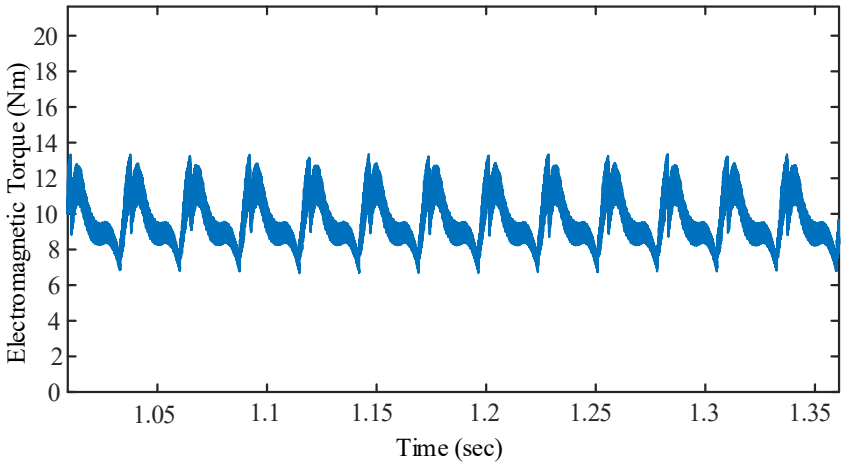

Figure 5.17(b): Variation of electromagnetic torque with time at 42 kmph

CONCLUSIONS

A multi-objective metaheuristic technique TLBO based controller is used for optimizing SRM drive performance vis-à-vis average torque, torque per unit copper losses and torque ripple. The proposed technique is used to compute the optimal turn-on and turn-off angles of the stator phase windings to maximize the multi-objective function comprising the SRM drive performance indices. Two real time controllers are used to tune the turn-on and turn-off angles of the stator phase windings to obtain multiple desired objectives simultaneously. The optimal value of turn-on and turn-off angles are used to generate the gate pulses for the converter switches. The case studies and results show the marked improvement in the SRM drive performance indices and validate the effectiveness of the proposed technique.

Another TLBO based controller is used for optimizing the SRM drive performance when subjected to the Indian Drive Cycle (IDC). It computes the optimal turn-on and turn-off angles of the stator phase windings to maximize the multi-objective function comprising the SRM drive performance indices like average torque, stator copper losses and integral squared speed error. The optimal value of turn-on and turn-off angles are used to generate the gate pulses for the converter switches. Two real time controllers are used to tune the turn-on and turn-off angles of the stator phase windings to obtain multiple desired objectives simultaneously. The case studies and results show that the SRM tracks the drive cycle speed satisfactorily, while optimizing the drive performance indices. This validates the proposed technique.

SCOPE FOR FUTURE WORK

1. Application of other drive cycle (e.g. US07, NEDC, etc) on the SRM Drive.
2. Optimising SRM Drive using latest optimization tool e.g., Grey Wolf Optimiser.
3. Performance Optimisation using new converter topology e.g., MMC based asymmetric converter.

REFERENCES

[1]. Z. Yang, F. Shang, I. P. Brown, and M. Krishnamurthy, "Comparative Study of Interior Permanent Magnet, Induction, and Switched Reluctance Motor Drives for EV and HEV Applications," in IEEE Transactions on Transportation Electrification, vol. 1, no. 3, pp. 245-254, Oct. 2015.

[2]. A. Pop, T. Rusu, R. Martis, F. Pop Piglesan, I. Vintiloiu and C. Martis, "Optimal Design of SRMs for Comparable Output with PMSMs," IECON 2018 - 44th Annual Conference of the IEEE Industrial Electronics Society, 2018, pp. 5716-5722.

[3]. A. Emadi, *Advanced Electric Drive Vehicles*, Boca Raton, FL: CRC Press, Oct. 2014.J. A. Makwana, P. Agarwal, and S. P. Srivastava, "Novel simulation approach to analyses the performance of in-wheel SRM for an Electrical Vehicle," 2011 International Conference on Energy, Automation and Signal, 2011, pp. 1-5.

[4]. R. Krishnan, “Switched Reluctance Motor Drives: Modeling, Simulation, Analysis, Design, and Applications”, CRC Press, 2001.

[5]. B Bilgin, JW Jiang, A Emadi , “ Switched reluctance motor drives: fundamentals to applications” ,CRC Press,2019.

[6]. Zhenguo Li, Yabiao Wang, Hashing Qi and Jin-Woo Ahn, "SRM torque ripple minimization based on modified multi-level converter," 2008 International Conference on Electrical Machines and Systems, 2008, pp. 3374-3379.

[7]. Russa K, Husain I and EIbulukt M, “Torque ripple minimization in switched reluctance machines over a wide speed range,” *IEEE Transactions on Industry Applications,* vol. 34, pp. 1105-1112, Sep-Oct. 1998

[8]. Iqbal Husain and M Ethsani, “Torque ripple minimization in switched reluctance motor drives by PWM current control,” *IEEE Transactions on Power Electronics,* vol. 11, pp. 83-88, Jan. 1996.

[9]. X. D. Xue, K. W. E. Cheng and N. C. Cheung, "Evaluation of torque sharing functions for torque ripple minimization of switched reluctance motor drives in electric vehicles," 2008 Australasian Universities Power Engineering Conference, 2008, pp. 1-6.

[10]. J. W. Jiang, B. Bilgin, B. Howey and A. Emadi, "Design optimization of switched reluctance machine using genetic algorithm," 2015 IEEE International Electric Machines & Drives Conference (IEMDC), 2015, pp. 1671-1677.

[11]. D. Patil, S. Wang and L. Gu, "Multilevel converter topologies for high-power high-speed

switched reluctance motor: Performance comparison," 2016 IEEE Applied Power Electronics Conference and Exposition (APEC), 2016, pp. 2889-2896.

[12]. C. Ma and L. Qu, "Multi-objective Optimization of Switched Reluctance Motors Based on Design of Experiments and Particle Swarm Optimization," in IEEE Transactions on Energy Conversion, vol. 30, no. 3, pp. 1144-1153, Sept. 2015.

[13].R. V. Rao, V. J. Savsani, D. P. Vakharia, “Teaching-learning-based optimization: a novel method for constrained mechanical design optimization problems”, *Computer-Aided Design,* 2011, 43(3), pp. 303-315.

PUBLICATIONS

1. Mohd Farhanuddin. Sikandar Khan and Suman Bhowmick, "*Performance Optimization of Switched Reluctance Motor Drive using TLBO based controller*," in Power, Control and Computing Technologies, (ICPC²T –2022).
2. Mohd Farhanuddin. Sikandar Khan and Suman Bhowmick, " *Performance Optimization of Switched Reluctance Motor Drive with Indian Drive Cycle using TLBO-based Controller*," in 4th International Conference on Energy, Power and Environment (ICEPE 2022)

AUTHOR'S BRIEF CV

Mohd Farhanuddin received his B. Tech in Electrical and Electronics Engineering from KIET Ghaziabad, UP, India. He is pursuing M.Tech. in Power Systems from Delhi Technological University since August 2020.His area of interest includes Motor Drive Technology in Electric Vehicle Integration, HVDC, FACT devices.